A numerical study of ocean surface-layer response to atmospheric shallow convection: Impact of cloud shading, rain, and cold pools

Pierre-etienne Brilouet, Jean-luc Redelsperger, Marie-Noëlle Bouin, Fleur Couvreux, Najda Villefranque

Quarterly Journal of the Royal Meteorological Society
April 2024, Volume 150, Issue 760, Part A., Pages 1401-1419
https://doi.org/10.1002/qj.4651
https://archimer.ifremer.fr/doc/00869/98109/

A numerical study of ocean surface layer response to atmospheric shallow convection: impact of cloud shading, rain and cold pool

Brilouet Pierre-Etienne [1, 2, *], Redelsperger Jean-Luc [2], Bouin Marie-Noëlle [2, 3], Couvreux Fleur [3], Villefranque Najda [3]

[1] LEGOS Université de Toulouse, IRD, CNRS, CNES Toulouse, France
[2] Univ Brest, CNRS, Ifremer, IRD, Laboratoire d'Océanographie Physique et Spatiale (LOPS) IUEM F29280 Plouzané, France
[3] CNRM Université de Toulouse Météo-France, CNRS Toulouse, France

* Corresponding author : Pierre-Etienne Brilouet, email address : pierre-etienne.brilouet@ird.fr

Abstract :

The response of the oceanic surface layer to atmospheric shallow convection is explored using realistic atmospheric large eddy simulations coupled with an oceanic 1D model with high vertical resolution. The effects of cloud shading, rain and enhanced heat loss due to gust fronts on the edge of cold pools and their interactions are investigated on a case study of the Cooperative Indian Ocean Experiment on Intraseasonal Variability /Dynamics of the Madden-Julian Oscillation experiment in the tropical Indian Ocean, during a suppressed phase of the Madden-Julian Oscillation. The conditions of low surface wind and strong solar heating result in diurnal warming of the oceanic surface of 2°C over a depth of 1 m. Analysis of specific periods covering the diurnal cycle show contrasting effects of the cloud shading, rain and turbulent heat fluxes under the cold pools on the sea temperature at surface and below. On the one hand, decreasing the solar radiation (cloud shading) results in slight cooling horizontally extended and penetrating down to 1 to 2 m depth, depending on the time of the day. On the other hand, turbulent heat fluxes enhanced up to 300 W m−2 by gusts and freshwater lenses due to rain act together and more locally. They isolate and strongly cool a thin inner layer at the surface, which eventually destabilizes the surface layer and propagates the cooling downward. The exact relative part and efficiency of these processes depend on the time evolution of the thermal stratification and vertical turbulent mixing in the oceanic upper layer. Surface cooling up to −0.5°C may occur in a few tens of minutes and last for several hours, mitigating significantly the effects of the diurnal warming over large extents.

Keywords : oceanic surface layer, atmospheric shallow convection, cloud shading, cold pool, freshwater lens, diurnal warm layer, large eddy simulation, CINDY-DYNAMO

1 | INTRODUCTION

In tropical regions, ocean–atmosphere (O–A) interactions are key features for weather and climate. They occur on a wide range of spatial and temporal scales, involve many processes in ocean and atmosphere as well as their couplings. Because of this complexity, it is difficult to disentangle the mechanisms at play, although their appropriate representation is fundamental for weather forecasting and climate modelling.

Their numerical and experimental studies have been the focus of international programs such as the Tropical Ocean and Global Atmosphere – Coupled Ocean–Atmosphere Response Experiment (TOGA-COARE; Webster and Lukas, 1992) or Cooperative Indian Ocean Experiment on Intraseasonal Variability /Dynamics of the Madden-Julian Oscillation (CINDY/DYNAMO; Yoneyama et al., 2013). Earlier studies have primarily examined the O-A interactions at seasonal scales, as for instance those related to monsoon regimes. More recently, O–A interactions at smaller scales have been shown to be of critical importance regarding the intra-seasonal and inter-annual climate variability (Woolnough et al., 2007; Bernie et al., 2008; Flato et al., 2013; Vitart et al., 2017). An important mode of intra-seasonal variability is the Madden–Julian Oscillation (MJO), a cloud and rainfall pattern near the equator that typically recurs every 30 to 60 days. The MJO predictability has been improved in the past decade (Kim et al., 2017), thanks to coordinated multi-model experiments (Vitart et al., 2017) and field campaigns (e.g. CINDY-DYNAMO). Part of this improvement stems from understanding that local coupled processes are critical in the preconditioning phase and the triggering of this large-scale phenomena (Seo et al., 2014; Chen et al., 2016; Jiang et al., 2020). Indeed, the response of surface exchanges to intra-seasonal convective anomalies has been shown to be central during the active phase of the MJO (de Szoeke et al., 2015) but the role of O–A interactions in the MJO initiation remains not fully understood (Moum et al., 2014).

The preconditioning phase of the MJO corresponds to a period of weak surface wind, leading to the occurrence of a oceanic warm stable layer, called a diurnal warm layer (DWL), characterized by sea surface temperature (SST) diurnal variability of several degrees with a maximum in the early afternoon. DWLs are typically a few meters deep with vertical temperature variations of up to several degrees. They horizontally extend over a thousand kilometers and persist for several days (Price et al., 1986; Fairall et al., 1996; Soloviev and Lukas, 1997; Bellenger and Duvel, 2009; Matthews et al., 2014). Although DWLs have an impact on the system at rather large spatio-temporal scales, the mechanisms at play and their role in O–A interactions are mostly local. Due to its thermal inertia, the time scale of ocean response to atmospheric perturbations is generally larger than that of continental surfaces (Clayson and Weitlich, 2007). However, in presence of DWL the ocean surface can react rapidly to atmospheric stimuli depending on the diurnal cycle phase and the ocean stratification, thus shortening the timescale of ocean response. Under the suppressed phase of the MJO, deep atmospheric convection is inhibited but shallow convection can be present and generate short-lived precipitation (e.g. Ruppert and Johnson, 2015). While the impact of the SST on the structure of the marine atmospheric boundary layer (MABL) and the cloud organization has been studied (Ruppert and Johnson, 2016), the effect of shallow atmospheric convection on the upper-ocean, particularly in the presence of a DWL, has not been studied to our knowledge. This is the main objective of this paper. This convective activity, although associated with a small cloud cover (typically less than 10%), can impact the ocean surface layer through different processes, among which: cloud shading decreasing the amount of incoming solar radiation, precipitation leading to salinity barrier layer and cold pools with wind gusts modifying surface turbulent fluxes.

Over continental surfaces, Lohou and Patton (2014) or Horn et al. (2015) observed a dynamical response of the atmospheric boundary layer to surface heterogeneities induced by partial cloud shading. Over oceanic regions, Gentine et al. (2016), using simulations with a prescribed SST, found a minor impact of cloud shading unless large convective systems are present. The particular oceanic conditions of a DWL might lead to different conclusions as the solar radiation absorption is the main heat source of the DWL growth.

In the Tropics, the daily evolution of the SST is also influenced by sub-daily variations of sea surface salinity (SSS), mostly due to rainfalls (e.g. Sprintall and Tomczak, 1992; Mignot et al., 2007). Strong salinity gradients in the first meters form a stably stratified layer, which makes the mixed layer shallower and isolate the surface heat exchange from the sub-surface mixing (e.g. Katsaros and Buettner, 1969; Price, 1979). In-situ observations have shown that these freshwater lenses can form quickly (20 to 40 min), extend laterally over several tens of kilometers and take several hours to dissipate (e.g. Soloviev and Lukas, 1996; Reverdin et al., 2012, 2020). Statistical large-scale studies confirmed that these lenses are due to rain and that their effect can persist up to 3 days (Henocq et al., 2010; Boutin et al., 2014). Based on drifter observations, salinity drops at the surface reach

0.5 psu for 30% of the cases and correspond to temperature drops of 0.2 to 0.4°C occurring typically one hour later (Reverdin et al., 2012).

The formation and spread of cold pools at the sea surface is another indirect effect of shallow convection on the ocean surface layer. Cold pools are generated by the downward motion of cold air induced by the evaporation of rain drops into an unsaturated environment. As observed by de Szoeke et al. (2017), a sharp air temperature decrease is associated to cold pools, followed by a gradual return to the initial state. At the surface, it spreads out horizontally and generates a gust front on its downwind side. The surface fluxes are therefore locally modified by the increased wind speed and O–A temperature gradient (Yokoi et al., 2014; Gentine et al., 2016). Even if the impact of cold pools on surface fluxes is well established, especially in weak wind conditions (e.g. Jabouille et al., 1996; Redelsperger et al., 2000; Giglio et al., 2017; Thompson et al., 2019) their effect on interactions between the convective MABL and the ocean surface layer have been under-explored. Shallow convective clouds induce weak although numerous cold pools with horizontal spreads of the order of a few kilometers and lifetimes of about one hour (Zuidema et al., 2012, 2017). As highlighted by Yokoi et al. (2014), based on observations, the turbulent heat fluxes associated with the cold pool can increase of 15-20 W m^{-2} and 30-70 W m^{-2} for the sensible and latent heat fluxes, respectively.

Currently, there are few numerical studies that focus on local-scale processes involved in O–A coupling system and most reference case studies mainly focus on only one of the two components of the coupled system. Conventionally, atmospheric reference cases developed for Large Eddy Simulations (LES) are based either on a prescribed SST that does not vary according the air–sea exchanges, or on prescribed surface fluxes directly. Based on atmospheric and oceanic observations collected during the DYNAMO field campaign (Yoneyama et al., 2013), Brilouet et al. (2021) built a numerical case-study to examine the O–A interactions during the occurrence of a DWL. Coupling an atmospheric LES model with a 1D ocean model allows to simulate the main O–A interactions with a realistic spatio-temporal variability of the SST and therefore of air—sea exchanges. A notable advance of this framework is the consistently closed energy budget of the simulation. In Brilouet et al. (2021), it has been highlighted that the MABL mean structure and the shallow cumulus convection are directly rooted to the air–sea exchanges. The presence of a DWL leads to a diurnal cycle of the MABL depth and of the cloud layer with a larger cloud cover and a deepening of the clouds in the late afternoon (Fig. 1). This coupled modelling O–A framework provides the opportunity to investigate the tight interplay between ocean surface layer structure, air–sea interaction, and shallow clouds.

This study aims at investigating in details the impact of fine-scale atmospheric processes related to precipitating shallow convection on the ocean surface layer when a DWL is present. In particular, a focus is given on the temperature and salinity evolution of the upper ocean layer at the cloud and cold pool scales. This analysis is carried out to disentangle the role of three effects of shallow convection: cloud shading, gust fronts associated to the cold pools and rain. The paper is organized as follows: the coupled simulation and the methodology used to analyze the effects of shallow convection on the ocean surface layer are described in Section 2. Section 3 presents the cloud and cold pool statistical characteristics. In section 4, extensive analysis of specific periods (nocturnal, morning, afternoon and evening) is given leading to a generalization of respective role of clouds and cold pools through a statistical approach described in Section 5. Our results are summarized and discussed in section 6.

2 | DATA & METHODS

2.1 | Description of the Coupled Simulation

An extensive description of the case-study, the available observations and the modelling framework of the ocean-atmosphere coupled system are given in Brilouet et al. (2021). Only key information is provided here. An atmospheric LES performed with the Meso-NH model (Lac et al., 2018) is coupled with horizontally independent 1D ocean model at each surface grid point. The prognostic evolution of the SST is predicted in each ocean column according to the interface fields given by the atmospheric LES. The simulation is run for 54 hours over a 30-km wide domain with a horizontal grid spacing of 50 m. The

ocean model used is based on a prognostic equation of the turbulent kinetic energy (TKE) with a 1.5-order closure (Gaspar et al., 1990; Lebeaupin Brossier et al., 2009). In order to reproduce properly the surface layer, the ocean vertical grid is composed of a constant 10-cm grid mesh from the surface down to 5-m depth and then a progressively stretched grid mesh down to 300 m. The present analysis focuses on specific periods of the second day (see section 2.2).

Figure 1 illustrates the well-marked diurnal cycle for both atmospheric and ocean boundary layers that encompasses cloud, surface (through the SST and the net shortwave radiation SW_{net}) and oceanic mixing layer temperature along the 54 hours of simulation. On the one hand, the cloud layer structure is tightly rooted to the SST through the surface turbulent fluxes and its evolution is consistent with previous studies (Ruppert and Johnson, 2015, 2016). On the other hand, the structure of the ocean mixing layer is closely driven by the penetrating shortwave radiative flux. The main processes competing in the DWL growth and collapse include thus i/ solar radiation, ii/ turbulent transport and iii/ surface heat loss (see details in Brilouet et al. (2021)). Given the light wind conditions, we assume that the impact of the wave state on turbulent fluxes can be neglected. In the present case, the surface wind stress, though relatively weak, plays a crucial role in initiating turbulent vertical mixing. This mixing arises from the shear within the ocean surface layer, which transports downward the radiative energy accumulated close to the surface, contributing to the deepening of the DWL during the day. At the air–sea interface, the ocean layer loses energy through the non-solar heat fluxes. The duration and intensity of the DWL are deeply sensitive to this surface cooling. As noticed in Brilouet et al. (2021), downward SW radiative flux experiences a phase shift of approximately 4 hours relative to SST diurnal cycles, in agreement with observational studies (Price et al., 1986; Shinoda, 2005; Kawai and Wada, 2007). The simulated DWL decay at sunset is however slower than observed. As the potential contribution of waves to the ocean turbulent mixing has been neglected, this deserves to be explored in order to understand the persistence of the DWL in the late afternoon.

In order to properly outline the mechanisms at play, the equations of ocean mixing layer temperature in a 1-D framework are given below. The temperature tendency (TEND) can be decomposed into a volume source of energy (DT_SW) and a term of vertical mixing ($TURB$):

$$\underbrace{\frac{\partial T}{\partial t}}_{TEND} = \underbrace{\frac{SW_{net}}{\rho_0 c_p}\frac{\partial I}{\partial z}}_{DT\_SW} \underbrace{- \frac{\partial \overline{w'T'}}{\partial z}}_{TURB}, \tag{1}$$

where ρ_0 and c_p are the reference density and specific heat at constant pressure of seawater. The source of energy, DT_SW, is the radiative heating rate, with $I(z)$ the vertical transmittance of the SW. The direct cloud shading effect on the ocean surface layer is directly represented by DT_SW. At the air-sea interface, the boundary condition imposed on $TURB$, is expressed in terms of the non-solar surface heating flux (F_{nsol}):

$$-\overline{w'T'}(z=0) = \frac{F_{nsol}}{\rho_0 c_p}. \tag{2}$$

F_{nsol} is the sum of the surface sensible heat (H), latent heat (LE) fluxes and the net surface long-wave radiative flux (LW_{net}):

$$F_{nsol} = H + LE + LW_{net}, \tag{3}$$

Hereafter, F_{nsol} is counted positive when it denotes a gain of energy for the atmosphere (i.e., a loss of energy for the ocean). Each components of F_{nsol}, the upward long-wave radiative flux and turbulent (mainly latent) heat fluxes depend on the SST:

$$\begin{cases} H = -\rho_a c_{pa} C_H U_0 (SST - T_a), \\ LE = -\rho_a \mathcal{L}_v C_E U_0 (q_s(SST) - q_a), \\ LW_{net} \propto (SST)^4 - T_{rad}^4, \end{cases} \tag{4}$$

where ρ_a is the air density, c_{pa} the specific heat of moist air, U_0 the surface wind speed, T_a and q_a are the temperature and the specific humidity in the atmospheric surface layer, $\mathcal{L}_v$ is the latent heat of seawater vaporization at sea surface, C_H and C_E are transfer coefficients and T_{rad} is the effective radiative temperature of the atmosphere. The boundary condition (cf. Eq. 2) at the air-sea interface is therefore strongly dependent on the SST and on U_0. The momentum and turbulent heat fluxes are computed with the COARE 3.0 bulk parameterization (Fairall et al., 2003), which is perfectly adapted to the light-wind, tropical conditions of our study.

2.2 | Selection of Specific Periods

On the second day of the simulation, four periods of two hours were selected and are highlighted in Figure 1. As the simulated clouds correspond to shallow convection, their lifetime is less than an hour (Zuidema et al., 2012; Feng et al., 2015). For this reason, model has been run over these 4 periods in saving high-frequency outputs (every 2 min). The four selected periods are representative of the different phases of the DWL, from its growth to its dissipation. The 0400 LT - 0500 LT period represents the nocturnal regime with well-mixed conditions. The 0800 LT - 0900 LT period focuses on the growth phase associated with sunrise. The 1600 LT - 1700 LT period samples a well-established DWL characterized by strong stable stratification and a maximum SST. The 1900 LT - 2000 LT represents the dissipating phase of the DWL.

The analysis of the SST variability is challenging, given the nonlinear interplay of the intertwined mechanisms involved. In order to isolate the cloud shading and cold pool spreading, the detailed analysis of the processes at play will be done for two contrasted periods: the first one is at night (0400 LT – 0500LT) with no cloud shading effect while the second one is on the morning (0800 LT – 0900 LT), following sunrise during the DWL growth phase. We did not identify any configuration featuring a cloud with a significant shading effect but devoid of cold pools. Such a scenario does not exist since a substantial shading effect necessitates the presence of a sufficiently developed convective cloud, inevitably leading to precipitation, even light, generating thus a cold pool. For each time interval, a spatial zooming is performed to focus on a specific convective cloud and its associated cold pool. The high sampling frequency of the atmospheric and oceanic fields, combined with the high spatial resolution, enables us to closely monitor the changes in surface fluxes and the evolution of the ocean mixing layer. This level of temporal and spatial details was found mandatory, as despite their brief lifespans these atmospheric structures are able to induce long-lasting changes in the ocean mixing layer.

2.3 | Cloud and Cold Pool Identification Method

The clouds and cold pools have been identified using an object identification method described in Brient et al. (2019) and Villefranque et al. (2020). Brient et al. (2019) used it to identify up- and downdrafts and Villefranque et al. (2020) used it to identify shallow clouds. Also, Rochetin et al. (2021) applied the method to detect cold pools and proposed a conceptual model for convective density currents. In the following, this method is used to identify shallow cloud shade (2D-imprint) and cold pools. The clouds are defined using the Liquid Water Path (LWP):

$$\{x, y\} \in \text{cloud} \quad \Leftrightarrow \quad LWP(x, y) > 0.01 \text{ g m}^{-2}, \tag{5}$$

The cold pools are defined as a negative anomaly, with respect to the average over the domain, of the virtual potential temperature (θ_v) at $z = 10$ m:

$$\{x, y\} \in \text{cold pool} \quad \Leftrightarrow \quad \theta'_v(x, y) < -0.3\,^{\circ}\text{C}. \tag{6}$$

The −0.3 °C threshold is consistent with the typical lower range of the anomaly induced by shallow convection cold pools as reported in Zuidema et al. (2012). A distinction between active and dissipating cold pools is made based on the presence of a gust front at the edge. This gust front is defined by a surface wind speed deviation to the domain average $U'_0 > 2.5$ m s^{-1}. Figure 2 illustrates the clouds and cold pools detected with the object identification method. This approach enables us to assess various characteristics, including their quantity, size, thermodynamic properties, and the impact they have on air–sea interactions. A threshold of 1 km^2 or 400 grid cells, identical to Feng et al. (2015), is applied to filter out the small objects. Further on, only significantly large cloud and cold pools are selected. Given their small spatial extent and short lifetimes, the small objects are not considered to individually generate enough significant SW and F_{nsol} variations to impact the ocean mixing layer.

3 | CHARACTERISTICS OF THE CLOUD AND COLD POOL POPULATIONS

Figure 3 provides an overview based on hourly outputs of the population and characteristics of clouds and cold pools throughout the simulation duration. The parameter anomalies are calculated at a given time, with respect to the average over the entire domain.

A large number of very small clouds are simulated with an evolution in power scale. After filtering the smallest objects, 1% of the clouds are kept, representing about half (47%) of the cloud cover (Figs. 3a and 3b). Considering only the large clouds leads to a cloud cover of around 5% which is comparable to observations in the tropics under suppressed conditions (Feng et al., 2015). As shown in Fig. 3c, the smallest clouds have a negligible shading effect individually, while the large clouds can reduce the SW up to −400 W m^{-2}. Assuming that the LWP is related to the cloud vertical development, a higher vertical development leads to a stronger SW extinction (Fig. 3d).

The coverage fraction of cold pools presented in Fig. 3e exhibits a well-marked diurnal cycle while cloud number and fraction are fairly constant. The fraction is higher during the night when most of the active simulated cold pools are present. During the afternoon and the evening, dissipating cold pools are more prevalent. Interestingly, there is no direct link between the cold pools and their generating clouds in term of numbers and sizes. We can suppose that, once triggered by the rain evaporation, the cold pool evolution becomes uncoupled, and their spatial distribution depends on the thermodynamic conditions of the ABL. During the day, the cloud vertical extension is smaller (Fig. 1) leading to a small number of cold pools. Among these cold pools, most are small, as for clouds. So, filtering at 1 km^2 remove many cold pools while maintaining a fairly large domain coverage fraction. The size criterion is consistent with the active cold pool criterion (Fig. 3f). The influence of cold pools on the ocean mixing layer is measured through the anomaly of F_{nsol} averaged over the entire cold pool surface (Fig. 3g). Based on this metrics, for the entire population of cold pools, no clear impact on surface fluxes is observed with a quasi-gaussian symmetric distribution with a mean value of 6.9 W m^{-2}, a standard deviation of 33.7 W m^{-2} and a skewness of -0.057. Part of the cold pools are in a dissipating phase, characterized by stable conditions and a weaker mean wind; negative variation of F_{nsol} compared to the cold pool environment can thus be induced. Considering the large cold pools, the surface flux anomalies are slightly higher with a mean value of 17.1 W m^{-2}, the distribution is less spread out with a standard deviation of 21.4 W m^{-2}, and is skewed towards higher values (skewness of 0.4). The active cold pools, with a gust front, lead to an enhancement of the surface fluxes averaged over the entire cold pool with a mean value of 30.1 W m^{-2} and a standard deviation of 19.2 W m^{-2}. The distribution is broadly spread towards the higher values (skewness of 0.75) up to a maximum of 92.3 W m^{-2}. The cold pool

intensity can be characterised with the θ'_v anomaly (Fig. 3h). The more intense cold pools (up to $-0.7K$) present a gust front and have stronger F_{nsol} anomalies.

4 | DETAILED CASE STUDIES THROUGH THE DIURNAL CYCLE

4.1 | Nocturnal case study

Here, we focus the analysis on a cold pool identified from the virtual potential temperature deviation at 10 m (Fig. 4). In regard to the population of cold pools presented in Fig. 3, this cold pool is among the largest and most active ones. It lasts about one and a half hour and leads to a θ'_v perturbation of -1.35 K at 0434 LT. It propagates northwards and dissipates completely at 0600 LT. During its most intense spreading phase, the cold pool grows at the rate of 0.8 km^2 min^{-1} until reaching a size of 26.4 km^2. A gust front (purple contours on 10-m wind plot) is clearly identified on the northern boundary of this cold pool, in the direction of its propagation. The corresponding wind speed maximum is 7.3 m s^{-1} while the mean surface wind over the whole domain is 5 m s^{-1}. This increase of the local surface wind enhances the surface turbulent fluxes with a maximum of F_{nsol} up to 335 W m^{-2} inside the cold pool while the mean values are 214 W m^{-2} and 123 W m^{-2} over over the cold pool and the whole domain, respectively. This flux enhancement is clearly correlated to the gust front region and localized at its forward edge. In the cold pool core, stabilizing effects inhibit the turbulent mixing with low wind conditions and therefore weak surface turbulent fluxes. Regarding the evolution of the SST anomalies, a minimum of -0.6 K is reached at 0600 LT. While the cold pool expands in an almost circular manner, the SST anomaly patterns are elongated with the mean wind direction and look similar to the 20-min averaged rainfall pattern (red contours with a threshold of 0.1 g kg^{-1}). As shown below, the rainfall is indeed another process playing a key role in the behaviour of ocean surface layer.

Figure 5 illustrates the evolution of the ocean surface layer along a transect crossing the cold pool (green line in Fig. 4). Anomalies of up to -0.3 K and over a depth of 1 m are simulated. The temperature anomalies in the upper ocean are collocated with the patterns of rainfall. For this nocturnal case study, the oceanic temperature evolution is only driven by the turbulent mixing term ($TURB$) forced at the surface by F_{nsol}. In order to determine the stability conditions in the ocean surface layer, the Richardson number, defined as $Ri = N^2/S^2$ is computed (N being the buoyancy frequency and S the shear magnitude). Stable conditions are characterized by Ri > 1/4 (green dashed line for Ri=1/4) while unstable thermal conditions occur for Ri< 0 (brown dashed line for Ri = 0). Regions of Ri between 0 and 1/4 correspond to unstable dynamical conditions (surface shear). The surface imprint of 20-min cumulated rainfall is similar to the horizontal extension of the negative anomaly of turbulent mixing. By modifying the salinity vertical profile, rainfall induces a decrease of the sea water density over a thin layer. As observed on the Ri evolution, this thin layer is characterized by stable thermal conditions (Ri > 1/4) and is consequently decoupled from the ocean below. The surface ocean becomes more sensitive to the surface fluxes and able to cool more rapidly. The dynamical shear instabilities being relatively weak at this DWL stage, the turbulent mixing does not propagate this cooling downward, which remains trapped near the surface.

Figure 6 presents the time series of variables for a fixed grid point located in the cold pool illustrated on Fig. 4. The latent heat flux contributes the most to F_{nsol} whereas the sensible heat flux is almost negligible and the net longwave radiative flux induced only small variations. The variations of F_{nsol} are thus mainly driven by the wind intensity and moisture gradient at the sea surface. As the gust front of the cold pool is associated to a localized increase of wind module, the temporal evolution of F_{nsol} and U_0 are correlated as shown by the similar spatial variability of these parameters (Fig. 4). The rainfall peak at 0432 LT induces a rapid decrease of the salinity in the first 20 cm of ocean, decoupling this thin layer from the ocean below. Subsequently, the O-A interface is more reactive to the F_{nsol} and a decrease of the SST occurs, whereas ocean temperature at 20 cm decreases at 0440 LT, i.e. 8 minutes later. This is consistent with the mechanisms highlights during the nocturnal case study. The salinity

drop appears necessary to induce a modification of the oceanic temperature as the increase in F_{nsol} before 0430 LT does not impact the SST until the rain occurs. At 0450 LT, the cooling has been propagated downward at 20 cm depth forming a thin mixed surface layer. The minimum temperature of this layer is reached at 0600 LT with an anomaly of −0.4 K. The cooling affects a relatively thin layer (deeper than 40 cm and thinner than 2 m). While the ocean surface layer is destabilized in just a few minutes, it takes around three hours are necessary to return to an undisturbed state.

4.2 | Morning case study

The same analysis is repeated right after the sunrise (0600 LT). Over the period 0800 LT – 1000 LT, the SW radiative flux available at the sea surface under clear-sky conditions rises from 340 W m^2 to 775 W m^2. This 2-h period corresponding to light wind conditions ($\overline{U_0} \sim 1$ ms^{-1}), the ocean upper layer warms and the spatially averaged SST increases by 0.4 °C. The ocean upper layer gradually becomes thermally stable (Fig. 1c). At 0900 LT, after filtering out the smallest objects, 11 clouds are identified (for a total detected number of 638) covering 3.35 % of the whole simulation domain. In the same time, 19 cold pools are detected, 4 having areas larger than > 1 km^2), covering ∼ 3 % of the domain and 2 showing a marked gust front.

Figure 7 illustrates, on a sub-domain of 7 km × 7 km, the evolution of one identified cloud and its associated cold pool, from their formation up to their dissipation. The convective cloud moves northwards at a speed of 1.45 m s^{-1}, covering an area of 10.6 km^2 by 0900 LT with a lifespan of about 96 min. Generated by this cloud, the cold pool spreads northwards with a growth rate of 0.7 km^2 min^{-1} to reach its maximum area of 19.5 km^2 at 0900 LT. At its intensity peak, the cold pool is characterized by a θ_v perturbation of −1.2 K and a gust front with maximum wind intensity of 5.9 ms^{-1} located at its northern edge (purple contours in Figure 7). As during the night case, the F_{nsol} is locally enhanced by the gust front. At 0900 LT, F_{nsol} reaches a maximum of 275 W m^2 while the domain-averaged value is 119 W m^2. The evolution of the cold pool becomes rapidly decoupled from the cloud. The cloud shading (magenta contours on Figure 7) cuts off the net shortwave radiation at the surface. Following the diurnal cycle, the clear sky net shortwave radiation increases from 414 W m^2 to 713 W m^2 (domain average) between 0820 LT and 0940 LT. The cloud shading induces thus a strong reduction of the net surface shortwave radiation SW_{net} leading to a large apparent cooling. As during the night, the associated gust front increases the surface non-solar heating flux leading to the thin cool layer near the surface. Compared to the night period, the spatial imprint of the apparent cooling covers a larger area during the morning period.

The following analysis aims to investigate with more details how the ocean surface layer is modified by the cloud and associate cold pool. Time-height cross-sections of the main parameters driving the ocean surface layer are drawn along an axis (transect in Fig. 7) in Fig. 8. A negative temperature anomaly of −0.1 K at 50 cm starts at 0820 LT in phase with the SW_{net} cutoff. The cloud shading suspends the volumetric solar heating source DT_SW with an in-depth immediate impact on the sea temperature extending thus beyond the surface. Therefore, the negative temperature anomaly spreads vertically down to 1 m with a maximum intensity of −0.3 K. The cold pattern spreads horizontally over several kilometers. As the 1-D ocean model used here is not able to represent the horizontal advection and its effects, the apparent horizontal extent is only due to the effects of the cloud and cold pool propagating within the atmosphere along the considered axis. As for the nocturnal case study, the cold pool induces a surface cooling localized in a thin layer caused by the rain, making it more reactive to the increase of F_{nsol}. The turbulent mixing in the 0–50 cm layer is larger than for the night case and propagates the surface cooling down to 30 cm (cooling rate −0.6 °C h^{-1} to −1 °C h^{-1}). The combined effects of cloud shading and cold pool surface flux enhancement impact the ocean over a deeper layer compared to the nocturnal case where the strong cooling was confined near the surface (see Fig. 8d and 5c).

Figure 9 shows the high frequency evolution of relevant fields in the ocean and at the surface on a fixed point of the domain experiencing the passage of both cloud and cold pool. The separate roles of cloud shading and cold pool are difficult to disentangle. Due to cloud shading SW_{net} decreases nearly down to 0 from 0824 LT, i.e. 14 min before the rainfall. Related to

this heating decrease, the sea temperature uniformly decreases over a layer of at least 40 cm, illustrating that the cloud shading impacts the temperature more deeply than the cold pool. Even small clouds characterized by a LWP less than 700 g m^{-2} can have a significant shading. The cold pool effects highlighted for the night case are nevertheless also at play. The maximum of rainfall at 0838 LT leads to an abrupt decrease of the salinity at 20 cm, also slightly visible at 40 cm. The resulting decoupled layer being then more sensitive to the non solar flux, the ocean temperature decreases at the surface. The ocean temperature between the surface and 40 cm decreases homogeneously due to the shading effect between 0824 LT and 0840 LT (Fig. 9g). Then, rain creates a freshwater lens at the surface down to 20 cm (Fig. 9f, yellow). The surface heat loss due to F_{NSOL}, which is trapped in this layer, rapidly leads to a cooling from the surface down to 20 cm (Fig. 9g, yellow and green). The near surface mixing (Fig 8f) is not strong enough to break this stratification and to propagate the cooling downwards. Maximum temperature anomalies of −0.32 K and −0.28 K at the surface and 20 cm are reached between 0920 LT and 0930 LT. The recovery lasts for 1h30 to 2 h. Interestingly, the lowest temperature anomaly at 40 cm is reached at 1000 LT and this layer does not exhibit any recovery for at least the subsequent three hours.

The night case study highlighted that the rain-induced freshwater lens combined with the enhancement of turbulent fluxes in the cold pool gust front lead to a spatially localized large negative SST anomaly. In this case, the cooling remains confined to a thin layer near the surface. The comparison with the morning case shows that the cloud shading induces a cooling weaker than that due the cold pool but extending deeper in the ocean surface layer. The spatial extension of the resulting SST anomaly is also larger in the morning case than in the night case.

4.3 | Extension to the Afternoon and Evening Periods

Two additional time periods are now analyzed: one at the end of the afternoon (1600 to 1700 LT) when the DWL is established, and another one during the early evening (1900 to 2000 LT) when the DWL is dissipating. We focus on the differences with previous cases, in particular the impact of surface stratification due to the DWL.

The time evolution of the relevant fields in the ocean upper layer and at the surface is shown in Fig. 10 for fixed points experiencing the passage of cloud and cold pool.

At the beginning of the afternoon (1600 LT), the net solar flux is 520 W m^{-2} but declining rapidly. Even over a limited time period of 16 min, relatively shallow clouds ($LWP < 180 g m^{-2}$), leading to a maximum decrease of SW_{net} of 349 W m^{-2}, impact the ocean surface layer with a cooling rather homogeneously propagated from the surface down to 40 cm. The ocean surface layer is strongly stratified with a secondary thermocline at 60 cm depth and a temperature difference of 2.07°C between the surface and 2-m depth. The vertical turbulent mixing in this layer is strong (corresponding to cooling of −0.4 °C h^{-1}). The well-established DWL is more reactive to surface forcing than the well-mixed ocean surface layer found during the night. The combined effects of the rain and of the FN_{sol} enhanced by the gust front cool rapidly the upper layer up to −0.22°C in 40 minutes. This surface cooling destabilizes the layer above 20 cm and reinforces the mixing, which becomes strong enough to destabilize progressively the water column down to 1-m depth. The oceanic temperature is homogenized between the surface and 40 cm at 1800 LT with a recovery time shorter than for the morning period. Two differences with the morning case act together to make the cooling more homogeneous between the surface and 40 cm depth. First, the preexisting strong temperature stratification of the surface layer and the lower values of the solar heating enhance the decoupling and destabilization of the surface due to the freshwater lens. Second, a strong preexisting surface mixing propagates down the surface cooling more rapidly and efficiently (see the diurnal evolution of $TURB$ Fig.4 in Brilouet et al. (2021)).

The last period we investigated is after sunset when the DWL is slowly dissipating with an homogeneous temperature between the surface and 1.1 m. At the beginning of the period (1905 LT), a strong thermal stratification remains with a temperature difference of 1.36 °C between the surface and 2 m. Similarly to the nocturnal period, the ocean upper layer reacts

to the rain and cold pool passages with a SST anomaly decreasing independently of the temperature anomaly at 20 cm just after the formation of the thin barrier layer. After 10 min, the cooling due to heat loss in the ocean surface layer is nevertheless sufficient to destabilize it over a 20-cm depth. The turbulent mixing propagates the sea surface temperature anomaly down to 20 cm (yellow line, bottom panel of Fig 10k), progressively reducing the impact of the surface heat loss. In contrast with the afternoon case, the deeper upper layer makes the surface thermocline more difficult to erode. The cooling of the surface layer, which starts earlier than in the afternoon case, lasts also longer (yellow and blue profiles in Fig 10k).

5 | EXTENDED APPROACH THROUGH THE DIURNAL CYCLE

Summary of cooling effects attributed respectively to clouds and cold pools across the entire simulation domain is given for the four investigated time periods in Figure 11. The cooling of the SST (color of the inner symbol) and of the sea temperature at 40 cm (color of the outer ring) are represented for 226 clouds (38% for the evening case) and 53 cold pools (32% for the evening case). There is a remarkable homogeneity between the cooling associated to the clouds (square symbols) and to the cold pools (circles) whether or not the shading effect of clouds is present, confirming that most selected clouds are associated with cold pools.

To minimize redundancy, we optimize the number of independent cases by computing cooling effects within 20-min intervals (10 min before and 10 min after the given hour). Three one-hour periods are extracted from high resolution (2 minutes) outputs as investigated in the previous sections. For a given object at a given time, the anomaly of the solar radiation SW_{net} (negative) is computed as the spatial minimum of anomalies over the object on the 20 min interval. The anomalies of non solar flux FN_{sol} and rain amount (both positive) are computed similarly at the spatial maximum. The anomalies of temperature (cooling effect) is computed as solar radiation anomalies but corrected from the time evolution of the mean temperature over the domain on considered period.

The combined role of the rain and anomaly of FN_{sol} is striking in the night and evening time periods (Fig. 11a and 11d). Only when rain is present, SST decreases of more than 0.3 °C. If not, non solar flux anomalies of more than 60 W m^{-2} result in cooling of less than 0.05°C. This illustrates the effect of the barrier layer due to rain exacerbating the effect of surface heat loss by isolating it from the water below. At 40 cm conversely, there is no detectable role of rain, as the destabilizing effect of freshwater at the surface is too weak or happens too late to trigger mixing able to reach 40 cm (maximum cooling 0.16°C). For a given value of the non solar flux, the same amount of rain (symbol size) results in less cooling of the SST in the evening than at night (Fig 11a). This is the consequence of the surface turbulent mixing, which is much stronger during the evening than at night (intensity of vertical mixing is indicated on each subplot of Fig. 11). It makes the destabilizing effect of the freshwater lens less efficient by distributing it downwards ultimately diluting the cooling effect.

During time periods where the shading effect is present (Fig 11b and 11c), the SST cooling is linked to both anomalies of SW_{net} and FN_{sol}. Between 0800 and 0900 LT, strong cooling of SST (−0.2°C or more) corresponds to anomalies of F_{nsol} of 50 W m^{-2}, due to the cloud shading effect. Anomalies of SST similar to those of the night time period occur with similar non solar flux enhancement and less rain, due to the cutoff of solar radiation. However, it is not possible to disentangle the respective effects as the gradient of the cooling with respect to non solar flux and solar radiation anomalies are similar. The afternoon period presents significant differences with the morning one. First, the maximum SST cooling is weaker than during any other period, despite a strong effect of cloud shading (Fig 11c). Note than the largest SST cooling in the figure corresponds to the case study (cloud and cold pool) detailed in section 4.3. Except for this case, the rain effect combined with the anomaly of F_{nsol} is weak and very progressive compared to other cases. Second, the afternoon period is also the only one with no strong temperature gradients between the surface and 40 cm. That results from the very strong mixing at the surface (−0.41 °C h^{-1}). On the one hand, it prevents the freshwater anomaly to persist and to reinforce the effect of the anomaly of F_{nsol} at the surface. On the other

hand, it distributes the (weak) surface cooling down to 40 cm. The preexisting surface mixing (0 to 50 cm), which varies strongly throughout the DWL cycle is thus an important preconditioning factor of the combined effect of rain and enhancement of F_{nsol} both on the SST and temperature at 40 cm.

6 | CONCLUSIONS

The impact of shallow atmospheric convection on the ocean surface layer during a DWL event has been examined over the preconditioning non active phase of the MJO. In this phase, shallow clouds occur with short timescales, produce low rain rates, which are nevertheless sufficient to generate cold pools. These processes are explicitly resolved by an atmospheric LES model coupled at each grid point with a 1D ocean model able to reproduce the ocean surface layer processes. This framework, previously designed and validated in Brilouet et al. (2021), has been used to simulate two complete diurnal cycles. The fine spatial and temporal resolution enables a thorough exploration of the intricate interactions between the ocean surface layer, air–sea exchanges, and atmospheric convection, shedding light on the underlying mechanisms. The simulated shallow convective activity affects the ocean upper layer through several mechanisms: i/ Cloud shading reduces incoming solar radiation, thereby impacting heat absorption in depth. ii/ Rainfall contributes to the formation of a thin salinity barrier layer. iii/ Gusty cold pools modify surface turbulent fluxes.

During nocturnal conditions, at the leading edge of cold pools, wind gusts result in an increase of the non-solar heating flux, leading to a cooling of 0.3 K over a thin layer of about 50 cm. However, the magnitude of the cooling induced by the surface heat extraction (F_{nsol}) and its spatial extent is modulated by the rain patterns at the surface. The freshwater lenses due to rain form a shallow thermally stable layer close to the surface. This barrier layer, more reactive to a heat loss due to F_{nsol}, eventually destabilizes the surface and propagates the cooling downward. During the morning period, same processes are at play, but are concomitant to the cloud shading decreasing the SW radiative heating. The most substantial shading effects are linked to the largest clouds, which are almost always accompanied by a cold pool, leading to difficulties in disentangling the impact of the two effects. Nevertheless, the two processes result in different cooling effects. The cooling due to solar flux extinction is distributed vertically over a deeper layer (up to 1 m) and horizontally over larger areas than the cooling due to the combination of F_{nsol} and rain effects. The cloud shading effect is especially strong under the suppressed conditions considered in the case study with high solar radiation and light surface wind speed. In other situations, the impact of cloud shading on the ocean may be less substantial.

The apparent cooling due to the SW radiation absorption cut-off is distributed vertically over the entire surface layer. A larger cooling related to the cold pool due to the enhancement of turbulent surface fluxes is confined in the thin rain-induced barrier layer. While those processes occur over short time periods (about 30 min), the induced cooling on the ocean surface layer persists for several hours. Thus, although shallow clouds are small and short-lived, they can generate spatial variability of SST lasting over much longer time periods. The magnitude of the shallow convection effects on the ocean surface layer appears to be different along the DWL phase, due to the time evolution of the thermal stratification and vertical turbulent mixing. Extending the demonstrative night and morning period cases to the whole diurnal cycle does not enable to fully disentangle the involved mechanisms. Nevertheless, an analysis of all the cold pools and clouds covering more than 1 km^2 throughout the day confirms the results above. In the afternoon or in the evening, the vertical turbulent mixing in the ocean surface layer is stronger and becomes large enough to distribute downwards the surface cooling. The relative role of the freshwater lenses and surface heat loss in destabilizing the surface layer is weaker. The turbulent mixing in the surface layer, which varies strongly throughout the DWL cycle (Brilouet et al. (2021)) is a key preconditioning factor to have an efficient combined effect of rain and enhancement of F_{nsol} both on the sea surface temperature and below in the surface layer.

The present 1D-LES coupling framework used to study an observed DWL has allowed to explore the impact of the shallow

atmospheric convection on the ocean surface layer and on the SST. The analysis of the involved processes is complex due to the simultaneous and intertwined effects of cloud shading, rain and cold pools. To go further using the same tools, sensitivity tests based on idealized simulations would be a good way to decouple the effects of cloud shading, gust fronts in the cold pools and freshwater lenses. The mechanisms highlighted in the present study are based on a single, though robust case study. The effects of the stratification and of the vertical mixing in the oceanic surface layer have been shown to play a strong role in the intensity of the surface cooling and in the timing of its propagation downward. These surface conditions vary throughout a single day but also from day to day depending on the surface wind and phase of the MJO among others. Similar realistic studies, performed on other cases where shallow convection generating clouds and cold pools is present would help to generalize the findings of the present paper to other surface conditions. Finally, the present numerical framework presents also several limitations in representing realistically the radiative surface forcing and the response of the oceanic surface layer. First, using a 1D atmospheric radiative scheme as currently done in our LES configuration can induce artefacts due to the cloud shading being considered directly under the cloud. Taking into account the 3D radiative effects of the clouds might lead to slightly different spatial patterns of SW extinction (Jakub and Mayer, 2017; Villefranque and Hogan, 2021). Second, the present configuration uses a 1D oceanic model to reproduce the evolution of the DWL. This 1D view includes several simplifications concerning the representation of the turbulent mixing: neglecting 3D turbulence and lateral advection probably affects the time evolution of the mixing in our simulation, which has been found critical. In particular, Brilouet et al. (2021) noted that the SST decay at the end of the afternoon, in the DWL cycle, is significantly delayed in the simulation with respect to observations. One way to reduce this delay could be the adjustment of the turbulence scheme in the oceanic mixed layer. Another way pursued in a parallel ongoing work is the use of an oceanic LES on this case study, both allowing to solve this issue and opening the possibility to couple an atmospheric LES model with an oceanic LES model to reproduce explicitly the oceanic and atmospheric turbulent processes and the ocean-atmosphere interactions, within a comprehensive framework.

Finally, having a dedicated field campaign on shallow convection over the ocean, such as the Elucidating the role of clouds-circulation coupling in climate (EUREC^{4}A) campaign (Stevens et al., 2021) would be a considerable asset. Satellite observations, including data from spaceborne synthetic aperture radar (SAR) images, which provide information on sea surface roughness, can also be of great interest to investigate the air—sea interactions (Brilouet et al., 2023). Combining the numerical framework used here with in situ data and satellite observations can deeply strengthen the inferences about the mechanisms at play.

ACKNOWLEDGEMENTS

This work was supported by the French national research agency (Agence National de la Recherche) through the ANR-COCOA project “COmprehensive Coupling approach for the Ocean and the Atmosphere” (grant: ANR-16-CE01-0007).

DATA AVAILABILITY STATEMENT

The data that support the findings of this study are available from the corresponding author upon reasonable request.

REFERENCES

Hugo Bellenger and Jean-Philippe Duvel. An Analysis of Tropical Ocean Diurnal Warm Layers. *Journal of Climate*, 22(13):3629–3646, July 2009. doi: https://doi.org/10.1175/2008JCLI2598.1.

D. J. Bernie, E. Guilyardi, G. Madec, J. M. Slingo, S. J. Woolnough, and J. Cole. Impact of resolving the diurnal cycle in an ocean–atmosphere GCM. Part 2: A diurnally coupled CGCM. *Climate Dynamics*, 31(7-8):909–925, December 2008. doi: https://doi.org/10.1007/s00382-008-0429-z.

Jacqueline Boutin, Nicolas Martin, Gilles Reverdin, Simon Morisset, Xiaobin Yin, L Centurioni, and Nicolas Reul. Sea surface salinity under rain cells: Smos satellite and in situ drifters observations. *Journal of Geophysical Research: Oceans*, 119(8):5533–5545, 2014.

Florent Brient, Fleur Couvreux, Najda Villefranque, Catherine Rio, and Rachel Honnert. Object-Oriented Identification of Coherent Structures in Large Eddy Simulations: Importance of Downdrafts in Stratocumulus. *Geophysical Research Letters*, 46(5):2854–2864, March 2019. doi: https://doi.org/10.1029/2018GL081499.

P. Brilouet, D. Bouniol, F. Couvreux, A. Ayet, C. Granero-Belinchon, M. Lothon, and A. Mouche. Trade wind boundary layer turbulence and shallow precipitating convection: New insights combining sar images, satellite brightness temperature, and airborne in situ measurements. *Geophysical Research Letters*, 50(2):e2022GL102180, 2023. doi: https://doi.org/10.1029/2022GL102180.

Pierre-Etienne Brilouet, Jean-Luc Redelsperger, Marie-Noëlle Bouin, Fleur Couvreux, and Cindy Lebeaupin Brossier. A case-study of the coupled ocean–atmosphere response to an oceanic diurnal warm layer. *Quarterly Journal of the Royal Meteorological Society*, 147(736):2008–2032, 2021. doi: https://doi.org/10.1002/qj.4007.

Shuyi S. Chen, Brandon W. Kerns, Nick Guy, David P. Jorgensen, Julien Delanoë, Nicolas Viltard, Christopher J. Zappa, Falko Judt, Chia-Ying Lee, and Ajda Savarin. Aircraft observations of dry air, the itcz, convective cloud systems, and cold pools in mjo during dynamo. *Bulletin of the American Meteorological Society*, 97(3):405 – 423, 2016. doi: https://doi.org/10.1175/BAMS-D-13-00196.1.

Carol Anne Clayson and Derrick Weitlich. Variability of tropical diurnal sea surface temperature. *Journal of Climate*, 20(2):334–352, 2007. doi: https://doi.org/10.1175/JCLI3999.1.

Simon P. de Szoeke, James B. Edson, June R. Marion, Christopher W. Fairall, and Ludovic Bariteau. The MJO and Air–Sea Interaction in TOGA COARE and DYNAMO. *Journal of Climate*, 28(2):597–622, January 2015. doi: https://doi.org/10.1175/JCLI-D-14-00477.1.

Simon P. de Szoeke, Eric D. Skyllingstad, Paquita Zuidema, and Arunchandra S. Chandra. Cold pools and their influence on the tropical marine boundary layer. *Journal of the Atmospheric Sciences*, 74(4):1149 – 1168, 2017. doi: https://doi.org/10.1175/JAS-D-16-0264.1.

C. W. Fairall, E. F. Bradley, D. P. Rogers, J. B. Edson, and G. S. Young. Bulk parameterization of air-sea fluxes for Tropical Ocean-Global Atmosphere Coupled-Ocean Atmosphere Response Experiment. *Journal of Geophysical Research: Oceans*, 101(C2):3747–3764, February 1996. doi: https://doi.org/10.1029/95JC03205.

Christopher Fairall, E. F. Bradley, J. E. Hare, A. A. Grachev, and J. B. Edson. Bulk Parameterization of Air–Sea Fluxes: Updates and Verification for the COARE Algorithm. *Journal of Climate*, 16(4):571–591, February 2003. ISSN 0894-8755, 1520-0442. URL https://doi.org/10.1175/1520-0442(2003)016<0571:BPOASF>2.0.CO;2.

Zhe Feng, Samson Hagos, Angela K. Rowe, Casey D. Burleyson, Matus N. Martini, and Simon P. de Szoeke. Mechanisms of convective cloud organization by cold pools over tropical warm ocean during the amie/dynamo field campaign. *Journal of Advances in Modeling Earth Systems*, 7(2):357–381, 2015. doi: https://doi.org/10.1002/2014MS000384.

G. Flato, J. Marotzke, B. Abiodun, P. Braconnot, S. C. Chou, W. Collins, P. Cox, F. Driouech, S. Emori, V. Eyring, C. Forest, P. Gleckler, E. Guilyardi, C. Jakob, V. Kattsov, C. Reason, and M. Rummukainen. *Evaluation of climate models*, pages 741–882. Cambridge University Press, Cambridge, UK, 2013. doi: https://doi.org/10.1017/CBO9781107415324.020.

Philippe Gaspar, Yves Grégoris, and Jean-Michel Lefevre. A simple eddy kinetic energy model for simulations of the oceanic vertical mixing: Tests at station Papa and long-term upper ocean study site. *Journal of Geophysical Research: Oceans*, 95(C9):16179–16193, 1990. ISSN 2156-2202. URL http://dx.doi.org/10.1029/JC095iC09p16179.

Pierre Gentine, Alix Garelli, Seung-Bu Park, Ji Nie, Giuseppe Torri, and Zhiming Kuang. Role of surface heat fluxes underneath cold pools. *Geophysical Research Letters*, 43(2):874–883, 2016. doi: https://doi.org/10.1002/2015GL067262.

Donata Giglio, Sarah T. Gille, Aneesh C. Subramanian, and San Nguyen. The role of wind gusts in upper ocean diurnal variability. *Journal of Geophysical Research: Oceans*, 122(9):7751–7764, 2017. doi: https://doi.org/10.1002/2017JC012794.

Claire Henocq, Jacqueline Boutin, Gilles Reverdin, François Petitcolin, Sabine Arnault, and Philippe Lattes. Vertical variability of near-surface salinity in the tropics: Consequences for l-band radiometer calibration and validation. *Journal of Atmospheric and Oceanic Technology*, 27(1):192–209, 2010.

GL Horn, HG Ouwersloot, J Vilà-Guerau De Arellano, and M Sikma. Cloud shading effects on characteristic boundary-layer length scales. *Boundary-Layer Meteorology*, 157(2):237–263, 2015. doi: https://doi.org/10.1007/s10546-015-0054-4.

P. Jabouille, J. L. Redelsperger, and J. P. Lafore. Modification of surface fluxes by atmospheric convection in the toga coare region. *Monthly Weather Review*, 124(5):816 – 837, 1996. doi: https://doi.org/10.1175/1520-0493(1996)124<0816:MOSFBA>2.0.CO;2.

F. Jakub and B. Mayer. The role of 1-d and 3-d radiative heating in the organization of shallow cumulus convection and the formation of cloud streets. *Atmospheric Chemistry and Physics*, 17(21):13317–13327, 2017. doi: https://doi.org/10.5194/acp-17-13317-2017.

X. Jiang, A. Adames, D. Kim, E. Maloney, H. Lin, H. Kim, C. Zhang, C. Demott, and N. Klingaman. Fifty years of research on the madden-julian oscillation: Recent progress, challenges, and perspectives. *Journal of Geophysical Research: Atmospheres*, page e2019JD030911, 07 2020. doi: https://doi.org/10.1029/2019JD030911.

Christina Katsaros and Konrad JK Buettner. Influence of rainfall on temperature and salinity of the ocean surface. *Journal of Applied Meteorology (1962-1982)*, pages 15–18, 1969.

Yoshimi Kawai and Akiyoshi Wada. Diurnal sea surface temperature variation and its impact on the atmosphere and ocean: A review. *Journal of Oceanography*, 63(5):721–744, October 2007. doi: https://doi.org/10.1007/s10872-007-0063-0.

Daehyun Kim, Hyerim Kim, and Myong-In Lee. Why does the mjo detour the maritime continent during austral summer? *Geophysical Research Letters*, 44(5):2579–2587, 2017.

C. Lac, J.-P. Chaboureau, V. Masson, J.-P. Pinty, P. Tulet, J. Escobar, M. Leriche, C. Barthe, B. Aouizerats, C. Augros, P. Aumond, F. Auguste, P. Bechtold, S. Berthet, S. Bielli, F. Bosseur, O. Caumont, J.-M. Cohard, J. Colin, F. Couvreux, J. Cuxart, G. Delautier, T. Dauhut, V. Ducrocq, J.-B. Filippi, D. Gazen, O. Geoffroy, F. Gheusi, R. Honnert, J.-P. Lafore, C. Lebeaupin Brossier, Q. Libois, T. Lunet, C. Mari, T. Maric, P. Mascart, M. Mogé, G. Molinié, O. Nuissier, F. Pantillon, P. Peyrillé, J. Pergaud, E. Perraud, J. Pianezze, J.-L. Redelsperger, D. Ricard, E. Richard, S. Riette, Q. Rodier, R. Schoetter, L. Seyfried, J. Stein, K. Suhre, M. Taufour, O. Thouron, S. Turner, A. Verrelle, B. Vié, F. Visentin, V. Vionnet, and P. Wautelet. Overview of the meso-nh model version 5.4 and its applications. *Geoscientific Model Development*, 11(5):1929–1969, 2018. doi: 10.5194/gmd-72811-1929-2018.

Lebeaupin Brossier, V. Ducrocq, and H. Giordani. Two-way one-dimensional high-resolution air–sea coupled modelling applied to mediterranean heavy rain events. *Quarterly Journal of the Royal Meteorological Society*, 135(638):187–204, 2009. doi: 10.1002/qj.338. URL `https://rmets.onlinelibrary.wiley.com/doi/abs/10.1002/qj.338`.

Fabienne Lohou and Edward G. Patton. Surface energy balance and buoyancy response to shallow cumulus shading. *Journal of the Atmospheric Sciences*, 71(2):665 – 682, 2014. doi: https://doi.org/10.1175/JAS-D-13-0145.1.

Adrian J. Matthews, Dariusz B. Baranowski, Karen J. Heywood, Piotr J. Flatau, and Sunke Schmidtko. The Surface Diurnal Warm Layer in the Indian Ocean during CINDY/DYNAMO. *Journal of Climate*, 27(24):9101–9122, December 2014. doi: https://doi.org/10.1175/JCLI-D-14-00222.1.

Juliette Mignot, Clement de Boyer Montégut, Alban Lazar, and Sophie Cravatte. Control of salinity on the mixed layer depth in the world ocean: 2. tropical areas. *Journal of Geophysical Research: Oceans*, 112(C10), 2007.

James N. Moum, Simon P. de Szoeke, William D. Smyth, James B. Edson, H. Langley DeWitt, Aurélie J. Moulin, Elizabeth J. Thompson, Christopher J. Zappa, Steven A. Rutledge, Richard H. Johnson, and Christopher W. Fairall. Air–Sea Interactions from Westerly Wind Bursts During the November 2011 MJO in the Indian Ocean. *Bulletin of the American Meteorological Society*, 95(8):1185–1199, August 2014. doi: https://doi.org/10.1175/BAMS-D-12-00225.1.

James F Price. Observations of a rain-formed mixed layer. *Journal of Physical Oceanography*, 9(3):643–649, 1979.

James F. Price, Robert A. Weller, and Robert Pinkel. Diurnal cycling: Observations and models of the upper ocean response to diurnal heating, cooling, and wind mixing. *Journal of Geophysical Research*, 91(C7):8411, 1986. doi: https://doi.org/10.1029/JC091iC07p08411.

Jean-Luc Redelsperger, Françoise Guichard, and Sylvain Mondon. A parameterization of mesoscale enhancement of surface fluxes for large-scale models. *Journal of Climate*, 13(2):402 – 421, 2000. doi: https://doi.org/10.1175/1520-0442(2000)013<0402:APOMEO>2.0.CO;2.

Gilles Reverdin, Simon Morisset, Jacqueline Boutin, and Nicolas Martin. Rain-induced variability of near sea-surface t and s from drifter data. *Journal of Geophysical Research: Oceans*, 117(C2), 2012.

Gilles Reverdin, Alexandre Supply, Kyla Drushka, EJ Thompson, William E Asher, and Antonio Lourenço. Intense and small freshwater pools from rainfall investigated during spurs-2 on 9 november 2017 in the eastern tropical pacific. *Journal of Geophysical Research: Oceans*, 125(2):e2019JC015558, 2020.

Nicolas Rochetin, Cathy Hohenegger, Ludovic Touzé-Peiffer, and Najda Villefranque. A physically based definition of convectively generated density currents: Detection and characterization in convection-permitting simulations. *Journal of Advances in Modeling Earth Systems*, 13(7), 2021. doi: https://doi.org/10.1029/2020MS002402.

Yanes H. Ruppert and Richard H. Johnson. Diurnally Modulated Cumulus Moistening in the Preonset Stage of the Madden–Julian Oscillation during DYNAMO*. *Journal of the Atmospheric Sciences*, 72(4):1622–1647, April 2015. doi: https://doi.org/10.1175/JAS-D-14-0218.1.

James H. Ruppert and Richard H. Johnson. On the cumulus diurnal cycle over the tropical warm pool. *Journal of Advances in Modeling Earth Systems*, 8(2):669–690, June 2016. doi: https://doi.org/10.1002/2015MS000610.

Hyodae Seo, Aneesh C. Subramanian, Arthur J. Miller, and Nicholas R. Cavanaugh. Coupled Impacts of the Diurnal Cycle of Sea Surface Temperature on the Madden–Julian Oscillation. *Journal of Climate*, 27(22):8422–8443, 11 2014. ISSN 0894-8755. doi: https://doi.org/10.1175/JCLI-D-14-00141.1.

Takeaki Shinoda. Impact of the Diurnal Cycle of Solar Radiation on Intraseasonal SST Variability in the Western Equatorial Pacific. *Journal of Climate*, 18(14):2628–2636, July 2005. doi: https://doi.org/10.1175/JCLI3432.1.

Alexander Soloviev and Roger Lukas. Observation of spatial variability of diurnal thermocline and rain-formed halocline in the western pacific warm pool. *Journal of physical oceanography*, 26(11):2529–2538, 1996.

Alexander Soloviev and Roger Lukas. Observation of large diurnal warming events in the near-surface layer of the western equatorial Pacific warm pool. *Deep Sea Research Part I: Oceanographic Research Papers*, 44(6):1055–1076, June 1997. doi: https://doi.org/10.1016/S0967-0637(96)00124-0.

Janet Sprintall and Matthias Tomczak. Evidence of the barrier layer in the surface layer of the tropics. *Journal of Geophysical Research: Oceans*, 97(C5):7305–7316, 1992.

B. Stevens, S. Bony, D. Farrell, F. Ament, A. Blyth, C. Fairall, J. Karstensen, P. K. Quinn, S. Speich, C. Acquistapace, F. Aemisegger, A. L. Albright, H. Bellenger, E. Bodenschatz, K.-A. Caesar, R. Chewitt-Lucas, G. de Boer, J. Delanoë, L. Denby, F. Ewald, B. Fildier, M. Forde, G. George, S. Gross, M. Hagen, A. Hausold, K. J. Heywood, L. Hirsch, M. Jacob, F. Jansen, S. Kinne, D. Klocke, T. Kölling, H. Konow, M. Lothon, W. Mohr, A. K. Naumann, L. Nuijens, L. Olivier, R. Pincus, M. Pöhlker, G. Reverdin, G. Roberts, S. Schnitt, H. Schulz, A. P. Siebesma, C. C. Stephan, P. Sullivan, L. Touzé-Peiffer, J. Vial, R. Vogel, P. Zuidema, N. Alexander, L. Alves, S. Arixi, H. Asmath, G. Bagheri, K. Baier, A. Bailey, D. Baranowski, A. Baron, S. Barrau, P. A. Barrett, F. Batier, A. Behrendt, A. Bendinger, F. Beucher, S. Bigorre, E. Blades, P. Blossey, O. Bock, S. Böing, P. Bosser, D. Bourras, P. Bouruet-Aubertot, K. Bower, P. Branellec, H. Branger, M. Brennek, A. Brewer, P.-E. Brilouet, B. Brügmann, S. A. Buehler, E. Burke, R. Burton, R. Calmer, J.-C. Canonici, X. Carton, G. Cato Jr., J. A. Charles, P. Chazette, Y. Chen, M. T. Chilinski, T. Choularton, P. Chuang, S. Clarke, H. Coe, C. Cornet, P. Coutris, F. Couvreux, S. Crewell, T. Cronin, Z. Cui, Y. Cuypers, A. Daley, G. M. Damerell, T. Dauhut, H. Deneke, J.-P. Desbios, S. Dörner, S. Donner, V. Douet, K. Drushka, M. Dütsch, A. Ehrlich, K. Emanuel, A. Emmanouilidis, J.-C. Etienne,

S. Etienne-Leblanc, G. Faure, G. Feingold, L. Ferrero, A. Fix, C. Flamant, P. J. Flatau, G. R. Foltz, L. Forster, I. Furtuna, A. Gadian, J. Galewsky, M. Gallagher, P. Gallimore, C. Gaston, C. Gentemann, N. Geyskens, A. Giez, J. Gollop, I. Gouirand, C. Gourbeyre, D. de Graaf, G. E. de Groot, R. Grosz, J. Güttler, M. Gutleben, K. Hall, G. Harris, K. C. Helfer, D. Henze, C. Herbert, B. Holanda, A. Ibanez-Landeta, J. Intrieri, S. Iyer, F. Julien, H. Kalesse, J. Kazil, A. Kellman, A. T. Kidane, U. Kirchner, M. Klingebiel, M. Körner, L. A. Kremper, J. Kretzschmar, O. Krüger, W. Kumala, A. Kurz, P. L'Hégaret, M. Labaste, T. Lachlan-Cope, A. Laing, P. Landschützer, T. Lang, D. Lange, I. Lange, C. Laplace, G. Lavik, R. Laxenaire, C. Le Bihan, M. Leandro, N. Lefevre, M. Lena, D. Lenschow, Q. Li, G. Lloyd, S. Los, N. Losi, O. Lovell, C. Luneau, P. Makuch, S. Malinowski, G. Manta, E. Marinou, N. Marsden, S. Masson, N. Maury, B. Mayer, M. Mayers-Als, C. Mazel, W. McGeary, J. C. McWilliams, M. Mech, M. Mehlmann, A. N. Meroni, T. Mieslinger, A. Minikin, P. Minnett, G. Möller, Y. Morfa Avalos, C. Muller, I. Musat, A. Napoli, A. Neuberger, C. Noisel, D. Noone, F. Nordsiek, J. L. Nowak, L. Oswald, D. J. Parker, C. Peck, R. Person, M. Philippi, A. Plueddemann, C. Pöhlker, V. Pörtge, U. Pöschl, L. Pologne, M. Posyniak, M. Prange, E. Quiñones Meléndez, J. Radtke, K. Ramage, J. Reimann, L. Renault, K. Reus, A. Reyes, J. Ribbe, M. Ringel, M. Ritschel, C. B. Rocha, N. Rochetin, J. Röttenbacher, C. Rollo, H. Royer, P. Sadoulet, L. Saffin, S. Sandiford, I. Sandu, M. Schäfer, V. Schemann, I. Schirmacher, O. Schlenczek, J. Schmidt, M. Schröder, A. Schwarzenboeck, A. Sealy, C. J. Senff, I. Serikov, S. Shohan, E. Siddle, A. Smirnov, F. Späth, B. Spooner, M. K. Stolla, W. Szkółka, S. P. de Szoeke, S. Tarot, E. Tetoni, E. Thompson, J. Thomson, L. Tomassini, J. Totems, A. A. Ubele, L. Villiger, J. von Arx, T. Wagner, A. Walther, B. Webber, M. Wendisch, S. Whitehall, A. Wiltshire, A. A. Wing, M. Wirth, J. Wiskandt, K. Wolf, L. Worbes, E. Wright, V. Wulfmeyer, S. Young, C. Zhang, D. Zhang, F. Ziemen, T. Zinner, and M. Zöger. EUREC^{4}A. *Earth System Science Data Discussions*, 2021:1–78, 2021. doi: 10.5194/essd-2021-18.

Elizabeth J. Thompson, James N. Moum, Christopher W. Fairall, and Steven A. Rutledge. Wind limits on rain layers and diurnal warm layers. *Journal of Geophysical Research: Oceans*, 124(2):897–924, 2019. doi: https://doi.org/10.1029/2018JC014130.

Najda Villefranque and Robin J. Hogan. Evidence for the 3d radiative effects of boundary-layer clouds from observations of direct and diffuse surface solar fluxes. *Geophysical Research Letters*, 48(14), 2021. doi: https://doi.org/10.1029/2021GL093369.

Najda Villefranque, Danny Williamson, Fleur Couvreux, Frédéric Hourdin, Jacques Gautrais, Richard Fournier, Robin J Hogan, Stéphane Blanco, and Victoria Volodina. Process-based climate model development harnessing machine learning: Iii. the representation of cumulus geometry and their 3d radiative effects. *Earth and Space Science Open Archive*, page 30, 2020. doi: https://doi.org/10.1002/essoar.10505088.1.

F. Vitart, C. Ardilouze, A. Bonet, A. Brookshaw, M. Chen, C. Codorean, M. Déqué, L. Ferranti, E. Fucile, M. Fuentes, H. Hendon, J. Hodgson, H.-S. Kang, A. Kumar, H. Lin, G. Liu, X. Liu, P. Malguzzi, I. Mallas, M. Manoussakis, D. Mastrangelo, C. MacLachlan, P. McLean, A. Minami, R. Mladek, T. Nakazawa, S. Najm, Y. Nie, M. Rixen, A. W. Robertson, P. Ruti, C. Sun, Y. Takaya, M. Tolstykh, F. Venuti, D. Waliser, S. Woolnough, T. Wu, D.-J. Won, H. Xiao, R. Zaripov, and L. Zhang. The subseasonal to seasonal (s2s) prediction project database. *Bulletin of the American Meteorological Society*, 98(1):163 – 173, 2017. doi: https://doi.org/10.1175/BAMS-D-16-0017.1.

Peter J Webster and Roger Lukas. Toga coare: The coupled ocean–atmosphere response experiment. *Bulletin of the American Meteorological Society*, 73(9):1377–1416, 1992.

S. J. Woolnough, F. Vitart, and M. A. Balmaseda. The role of the ocean in the madden–julian oscillation: Implications for mjo prediction. *Quarterly Journal of the Royal Meteorological Society*, 133(622):117–128, 2007. doi: https://doi.org/10.1002/qj.4.

Satoru Yokoi, Masaki Katsumata, and Kunio Yoneyama. Variability in surface meteorology and air-sea fluxes due to cumulus convective systems observed during cindy/dynamo. *Journal of Geophysical Research: Atmospheres*, 119(5):2064–2078, 2014. doi: https://doi.org/10.1002/2013JD020621.

Kunio Yoneyama, Chidong Zhang, and Charles N. Long. Tracking Pulses of the Madden–Julian Oscillation. *Bulletin of the American Meteorological Society*, 94(12):1871–1891, December 2013. doi: https://doi.org/10.1175/BAMS-D-12-00157.1.

Paquita Zuidema, Zhujun Li, Reginald J. Hill, Ludovic Bariteau, Bob Rilling, Chris Fairall, W. Alan Brewer, Bruce Albrecht, and Jeff Hare. On trade wind cumulus cold pools. *Journal of the Atmospheric Sciences*, 69(1):258 – 280, 2012. doi: https://doi.org/10.1175/JAS-D-11-0143.1.

Paquita Zuidema, Giuseppe Torri, Caroline Muller, and Arunchandra Chandra. A survey of precipitation-induced atmospheric cold pools over oceans and their interactions with the larger-scale environment. *Surveys in Geophysics*, 38(6):1283–1305, 2017. doi: https://doi.org/10.1007/s10712-017-9447-x.

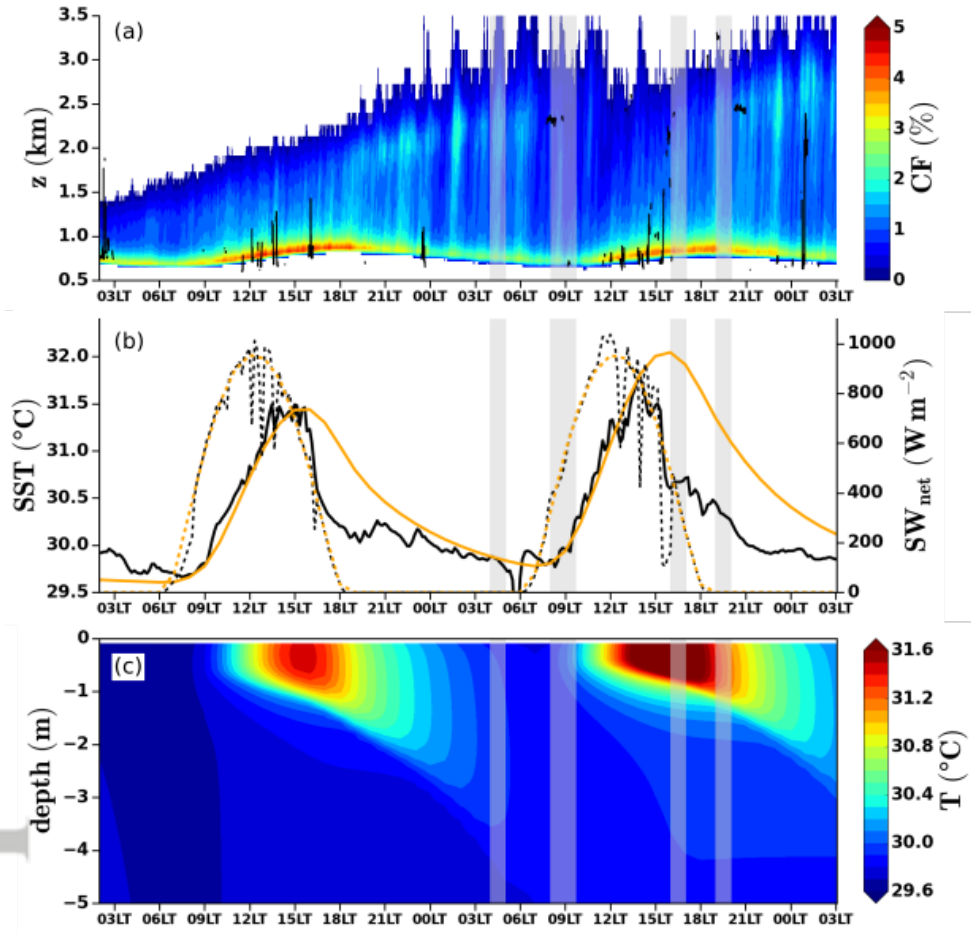

FIGURE 1 (a) Time–height cross-section of the simulated cloud cover with the observed cloud base (black) estimated from the ceilometer at the R/V Roger Revelle, (b) time series of the simulated sea surface temperature (solid orange) and net short-wave radiation (dashed orange) with the corresponding R/V Revelle observations (black) and (c) Time–depth cross-section of the temperature in the ocean mixed layer. The simulated fields are spatially averaged over the domain. The shaded areas correspond to focused periods with high-frequency outputs (every 2 min). (adapted from Brilouet et al. (2021)).

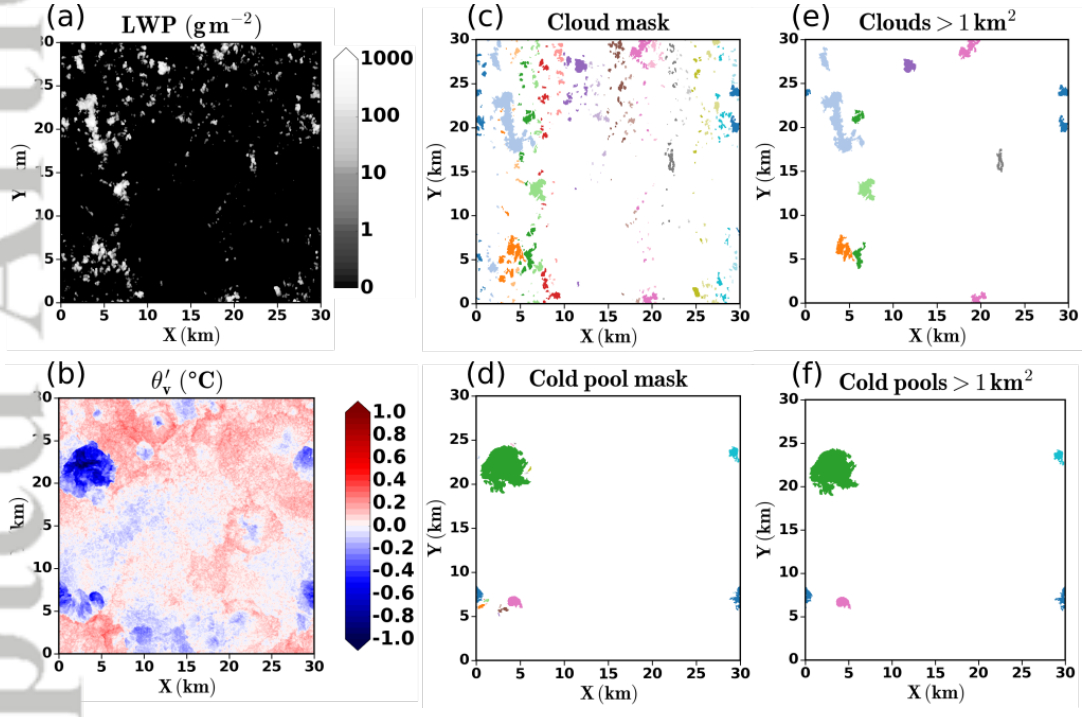

FIGURE 2 Horizontal cross-sections the Day 2 at 0900 LT of (a) the liquid water path and of (b) the virtual potential temperature fluctuations at 10 m, and the associated (c) clouds and (d) cold pools detected with an object-oriented identification (see text for details). In (e) and (f), the objects smaller than 1 km^2 have been filtered out.

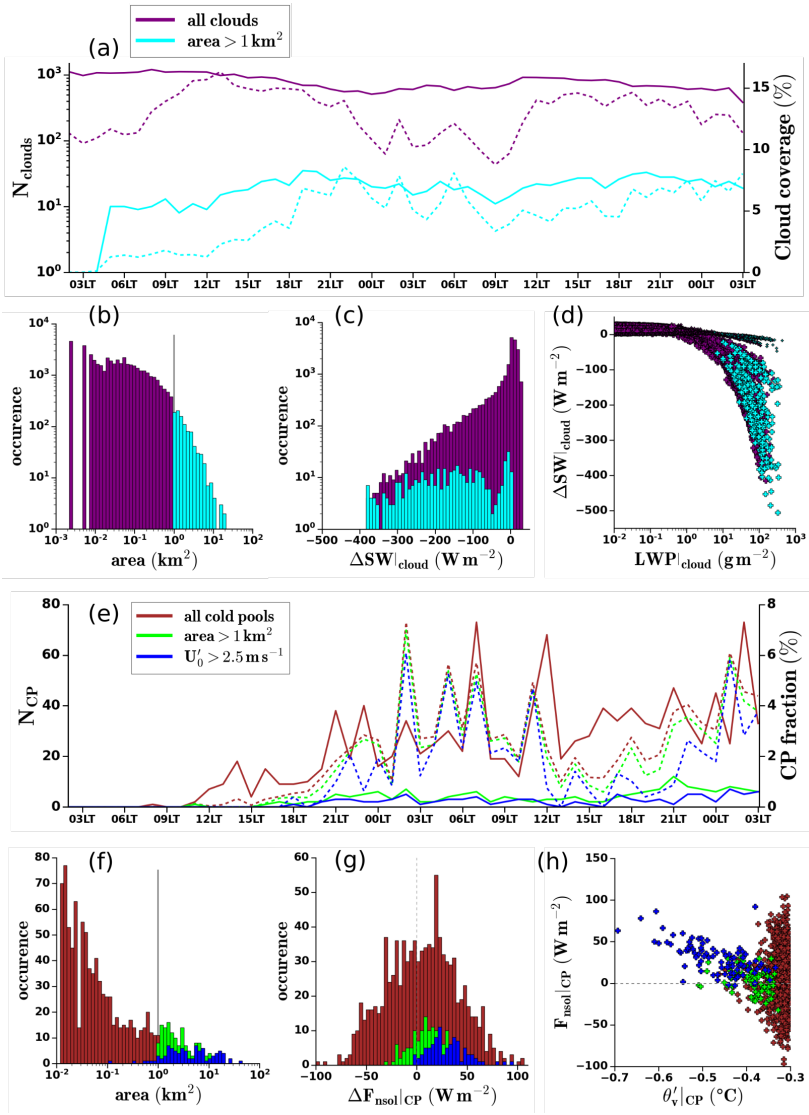

FIGURE 3 Cloud and cold pool characteristics along the entire simulation period: (a) time series of the number of clouds (solid lines) and the cloud cover (dashed lines), the purple lines refer to the entire set of objects identified as clouds and the cyan lines represent the large objects (area > 1 km^2), (b) distributions of cloud areas, the vertical gray line represents the filter at 1 km^2, (c) distribution of the short-wave radiation anomalies under the clouds, (d) short-wave radiation anomalies as a function of the liquid water path of clouds, smaller symbols correspond to 1 h after sunrise and 1 h before sunset (e) time series of the number of cold pools (solid lines) and the covered domain fraction (dashed lines), the brown lines refer to the entire set of objects identified as cold pools, the green lines represent the large objects (area > 1 km^2) and the blue lines correspond to cold pools with a gust front (U_0' > 2.5 m s^{-1}), (f) distributions of cold pool areas, the vertical gray line represents the filter at 1 km^2, (g) distribution of the non-solar heating flux anomalies under the cold pools, (h) non-solar heating flux anomalies as a function of the cold pool virtual potential temperature anomalies. The parameters $\Delta\ SW|_{cloud}$, $LWP|_{cloud}$, $\Delta\ F_{nsol}|_{CP}$ and $\theta_v'|_{CP}$ are averaged values over the detected objects.

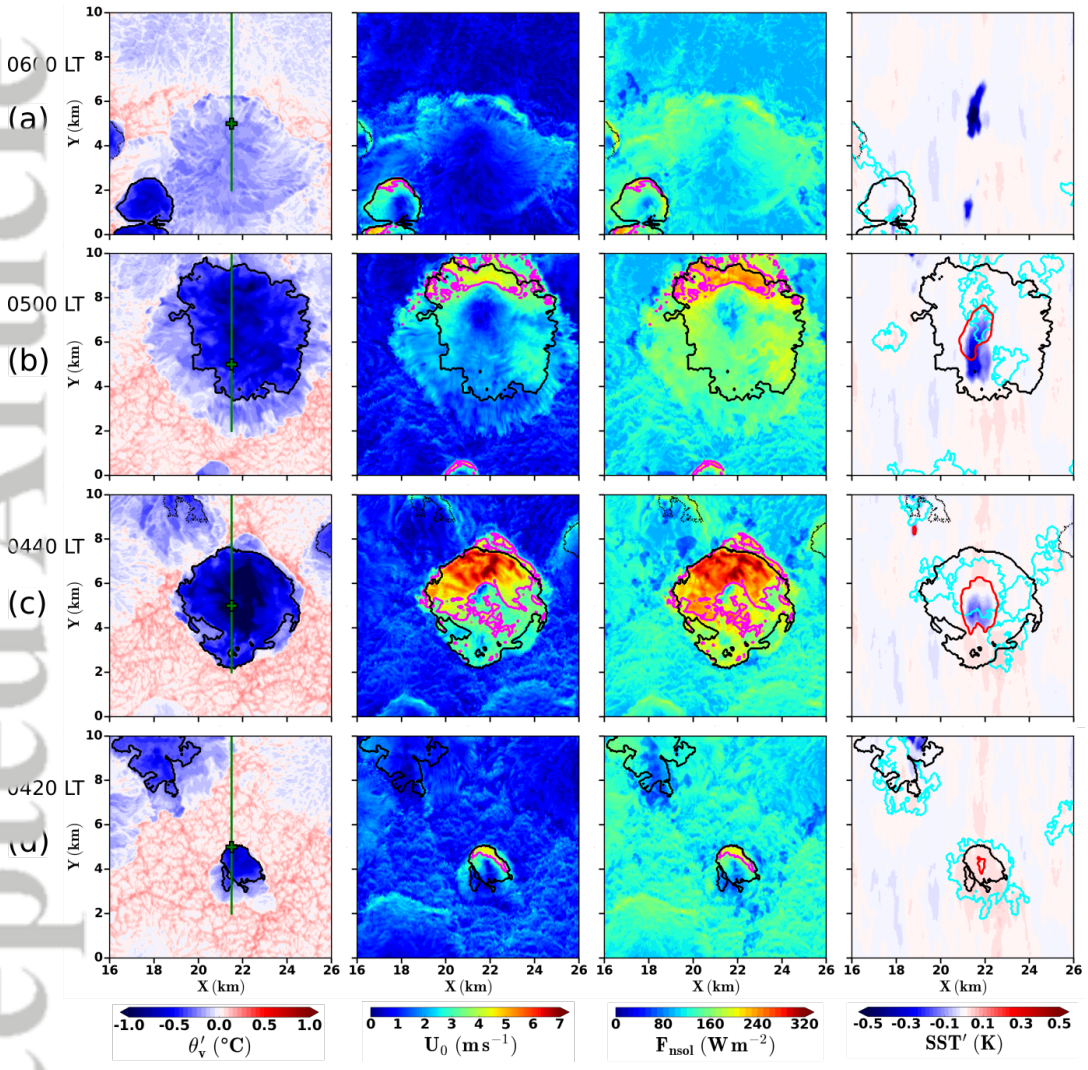

FIGURE 4 Horizontal cross-sections tracking the life cycle of a cold pool on a sub-domain of 10 km × 10 km during the nocturnal period of Day 2. From bottom to top, each snapshot are sketched at 20-min interval. From left to right: virtual potential temperature anomaly at 10 m, wind speed at 10 m, surface non-solar heating flux and SST anomaly. The vertical green line and the green cross indicate the axis and the fixed point used in Fig. 5 and Fig. 6, respectively. The black contours represent the active cold pools (solid lines) and the dissipating cold pools (dashed lines), the magenta contours (only shown in the panels of wind speed and surface non-solar heating flux) correspond to the gust front and the cyan and red contours (only shown in the right panels) are the clouds and the 20-min averaged rain with a threshold of 0.1 g kg^{-1}, respectively.

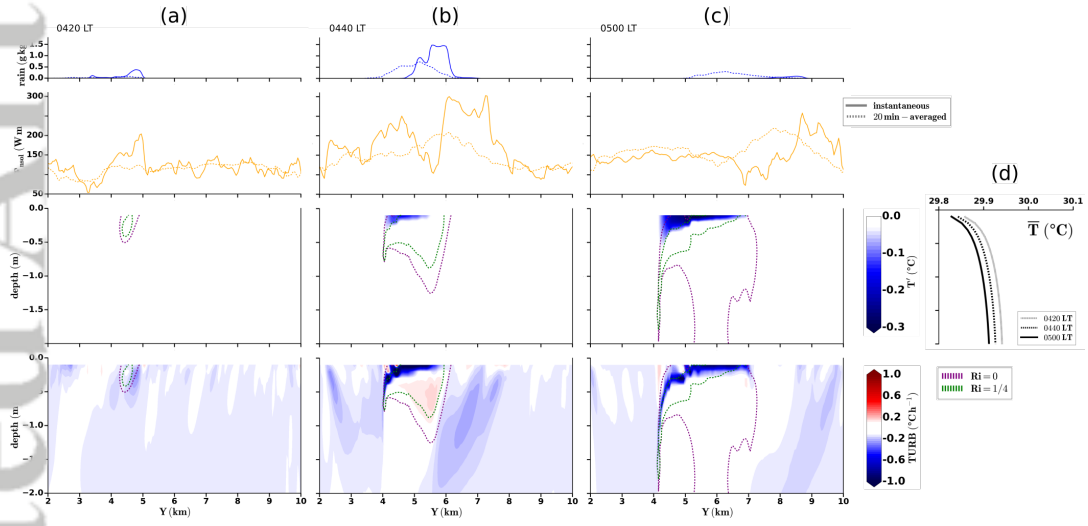

FIGURE 5 Vertical cross-sections of the ocean surface layer on the axis X = 21,5 km associated to the sub-domain zoom shown in Fig. 4. From left to right, each column is separated by 20 min. From top to bottom: transects along the Y section of instantaneous and 20-min averaged rain (blue) and non solar heating flux (orange) along the section, temperature anomaly in the ocean surface layer and vertical turbulent mixing ($TURB$). The purple and green dashed lines refer to $Ri = 0$ and $Ri = 1/4$, respectively. (d) Domain-averaged oceanic temperature profiles for the three times.

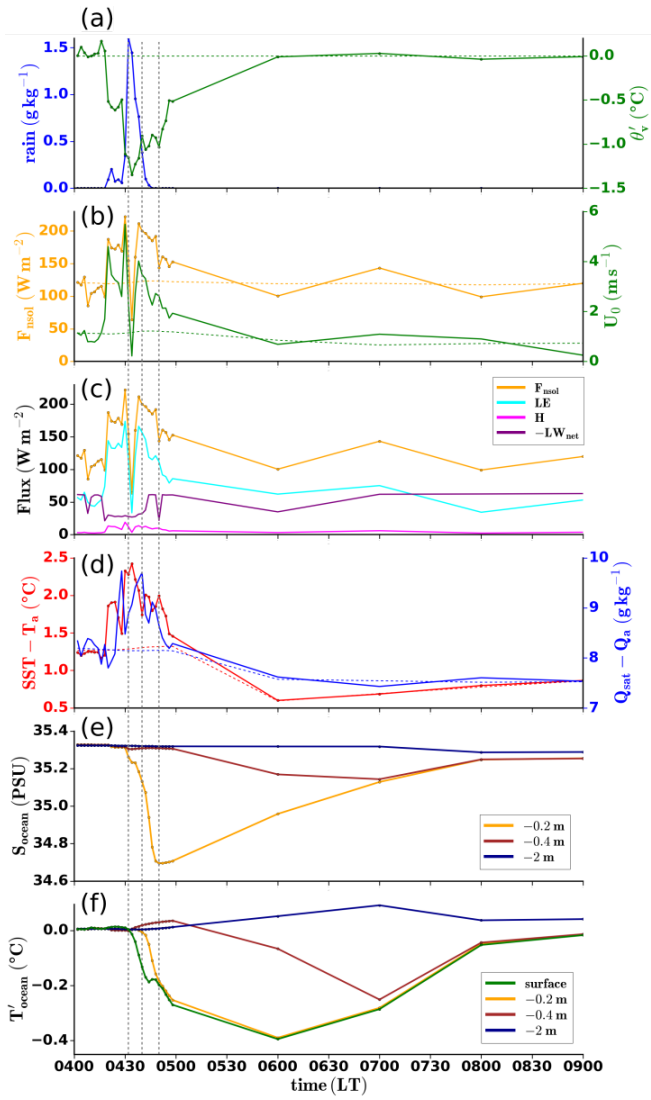

FIGURE 6 Time series on a fixed point (X = 21.5 km , Y = 5 km) associated to the sub-domain zoom, Fig. 4: (a) rain and θ'_v at 10 m, (b) F_{nsol} and U_0 at 10 m, (c) F_{nsol} and its components H, LE and $-LW_{net}$, (d) gradients of temperature and humidity between the surface and the first atmospheric model level, (e) salinity and (f) temperature anomalies in the ocean surface layer at different depths.

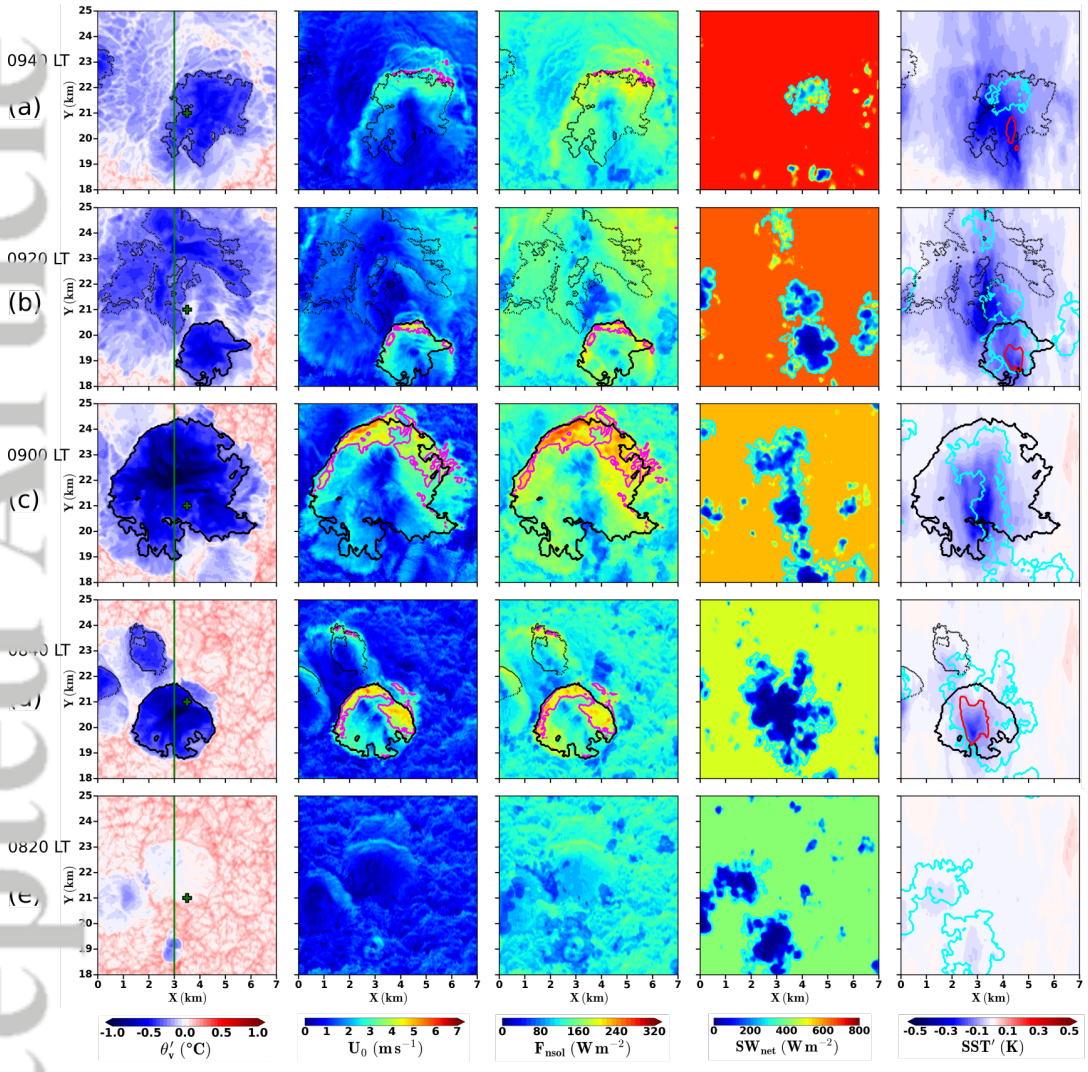

FIGURE 7 Horizontal cross-sections tracking the life cycle of clouds and associated cold pools on a simulation sub-domain of 7 km × 7 km in the morning of Day 2. From bottom to top, snapshots every 20 min. From left to right: virtual potential temperature anomaly at 10 m, wind speed at 10 m, surface non-solar heating flux, net shortwave radiation at the surface and SST anomaly. The vertical green line and the green cross indicate the axis and the fixed point used in Fig. 8 and Fig. 9, respectively. The black contours represent the active cold pools (solid lines) and the dissipating cold pools (dashed lines), the magenta contours correspond to the gust front, the cyan and the red contours represent the clouds and the 20-min averaged rain with a threshold of 0.1 g kg^{-1}, respectively.

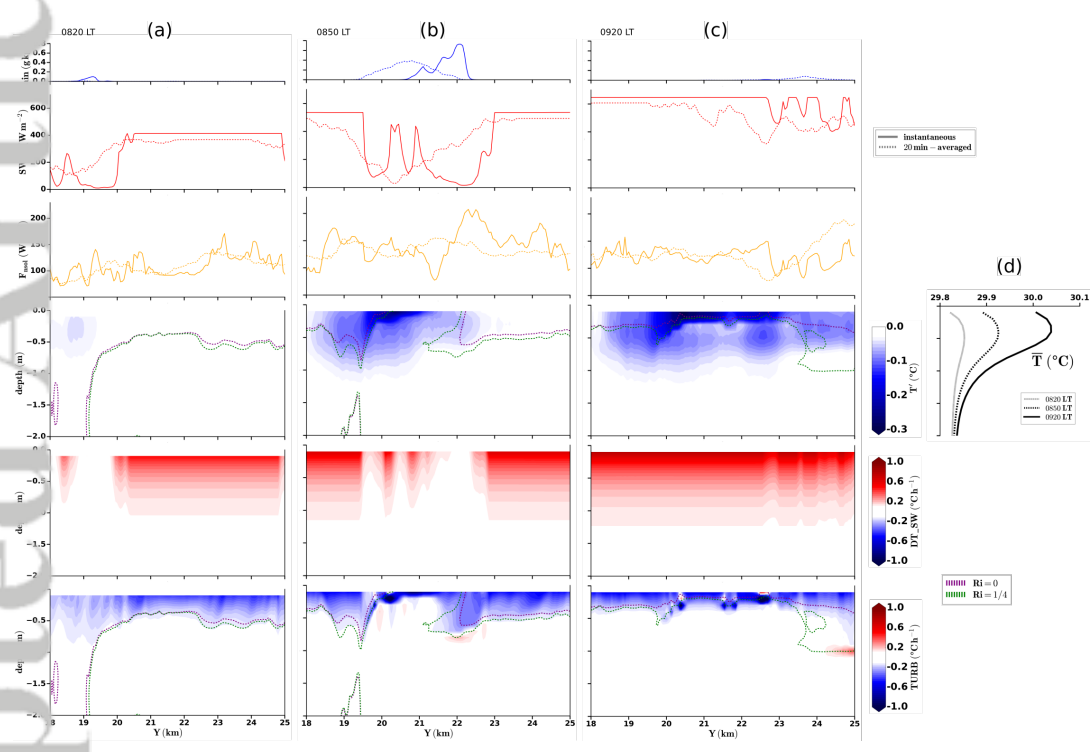

FIGURE 8 Vertical cross-sections of the ocean surface layer on the axis X = 3 km associated to the sub-domain zoom shown in Fig. 7. From left to right, snapshots every 30 min. From top to bottom: transects along the Y section of instantaneous and 20 min averaged rain (blue), net shortwave radiation (red) and non-solar heating flux (orange), temperature anomalies inside the oceanic mixing layer, absorbed SW radiation (DT_SW) and vertical turbulent mixing ($TURB$). The purple and green dashed lines refer to the $Ri = 0$ and $Ri = 1/4$, respectively. (d) The domain-averaged oceanic temperature profiles for the three times.

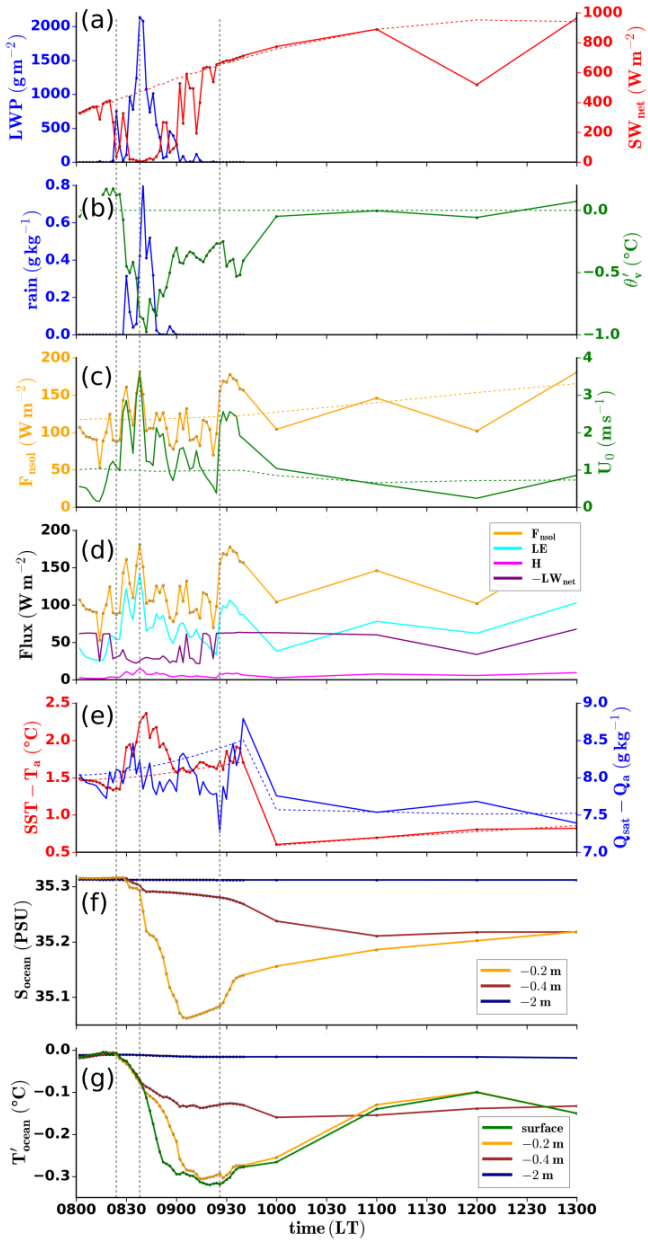

FIGURE 9 Time series on a fixed point (X = 3.5 km , Y = 21 km) associated to the sub-domain zoom shown in Fig. 7 of (a) LWP and SW_{net}, (b) rain and θ'_v at 10 m, (c) F_{nsol} and U_0 at 10 m, (d) F_{nsol} and its components H, LE and $-LW_{net}$, (e) gradients of temperature and humidity between the surface and the first model level, (f) salinity and (g) temperature anomaly in the ocean surface layer at different depths.

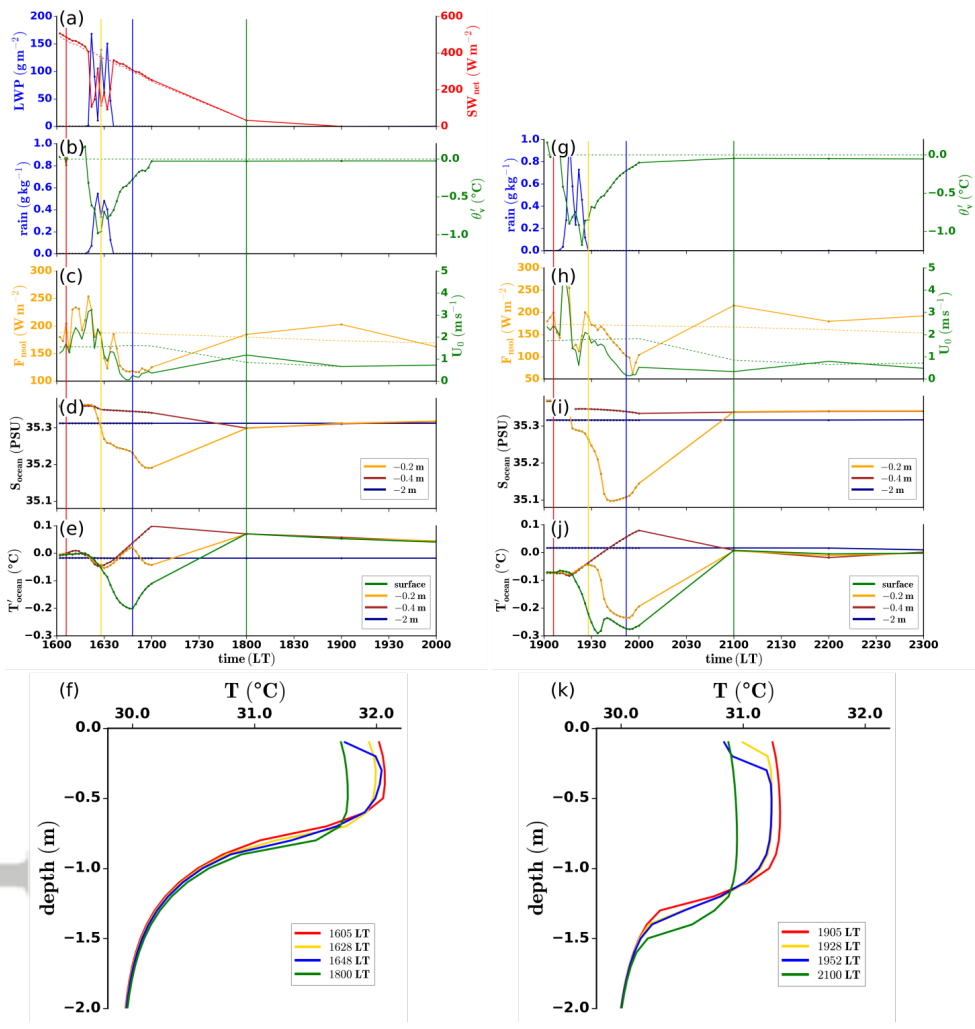

FIGURE 10 Time series on fixed points undergoing the passage of clouds and cold pools for the well established DWL (left column) and the dissipating phase of the DWL (right column). From top to bottom: (a) LWP and SW_{net}, (b,g) rain and θ'_v, (c,h) F_{rain} and U_0, (d,i) salinity and (e,j) temperature anomaly in the ocean surface layer at different depths. For each phase, (f,k) oceanic temperature profiles are plotted at specific times indicated by the vertical lines.

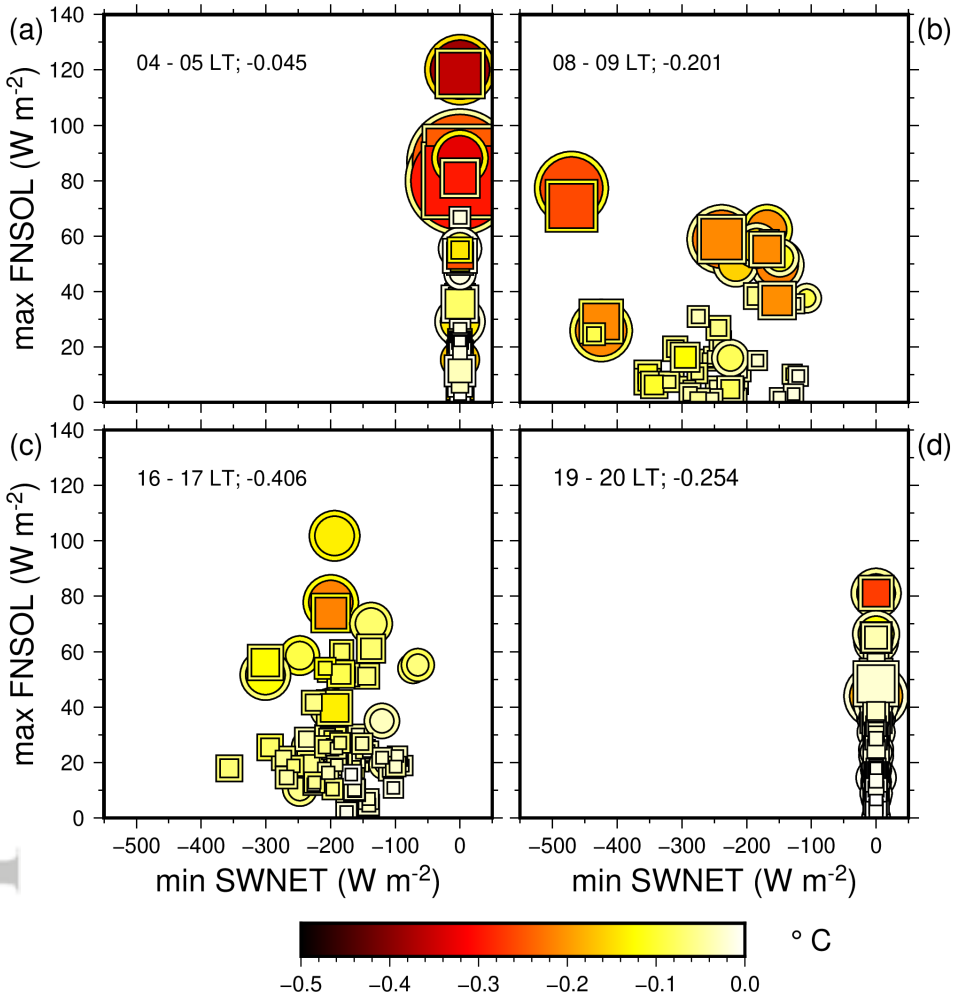

FIGURE 11 Scatterplots of the cooling (colour scale) induced by the cold pools (circles) and clouds (squares) as a function of the maximum anomaly of SW_{net} (x axis) and F_{nsol} (y axis). The size of the symbol corresponds to the maximum amount of rain, the colour in the inner part corresponds to the SST, the colour in the outer part corresponds to the temperature at 40 cm. In each subplot, the numbers after the time period indicate the mean vertical turbulent mixing (°C h^{-1}) over the 0–50 cm layer, at the middle of the time period.